Aalto University
School of Science
Engineering Physics

Rebecca Heilmann

Fabrication and characterisation of dielectric nanoparticle arrays

Tuning the light-matter interaction

Master's Thesis
Espoo, November 19, 2018

Supervisor: Professor Päivi Törmä, Aalto University
Advisor: Aaro Väkeväinen M.Sc. (Tech.)

Aalto University
School of Science
Engineering Physics

ABSTRACT OF
MASTER'S THESIS

Author:	Rebecca Heilmann		
Title:	Fabrication and characterisation of dielectric nanoparticle arrays Tuning the light-matter interaction		
Date:	November 19, 2018	**Pages:**	68
Major:	Engineering Physics	**Code:**	SCI3056
Supervisor:	Professor Päivi Törmä		
Advisor:	Aaro Väkeväinen M.Sc. (Tech.)		

Nanoparticles ordered in periodic arrays provide electromagnetic resonances called surface lattice resonances (SLRs) leading to a high degree of local field confinement. If dye molecules are added on top of the nanoparticle arrays the system can be in the strong coupling regime. Typically, nanoparticle arrays consist of metals which, however, provide very high losses. In contrast, high-index dielectrics are low-dissipative and can therefore lead to narrower SLRs and therefore to longer lifetimes.

In this work, we fabricate dielectric nanoparticle arrays made out of germanium and amorphous silicon. The SLRs of germanium and amorphous silicon nanoarrays are measured and compared to the SLRs of gold nanoarrays. A quality factor of up to 1.27 higher is provided by the SLRs of dielectric nanoarays compared to the SLRs of the gold nanoarrays. In addition, we measure the dispersion of the nanoarrays with fluorescent dye molecules on top and observe an indication of strong coupling.

Keywords:	plasmonics, strong coupling, quantum optics, dielectric nanoparticles, surface lattice resonances
Language:	English

Acknowledgements

This work for this Master's thesis was carried out at the Quantum Dynamics research group of the COMP Centre of Excellence at Aalto University.

First and foremost I would like to express my gratitude to Prof. Päivi Törmä for giving me the possibility to work in her group. I would also like to sincerely thank my supervisor Mr. Aaro Väkeväinen for his valuable guidance, advice and our discussions. Then, I would also like to thank the other guys from the QD group, Prof. Tommi Hakala, Dr. Konstantinos Daskalakis, Dr. Jani-Petri Martikainen, Mr. Antti Moilanen, Mr. Jani Taskinen, Mr. Marek Nečada and Mr. Alessandro Contrufo for all kinds of things, be for help with issues in the lab, insightful discussions over a lunch or practising my Finnish skills.

I would also like to thank my friends I made along my way in Finland and in Germany for great times and always reminding me that there is a life beneath studying.

I am grateful for the endless support my parents gave me throughout the best and worst times, without them I would not be the person that I am right now - Danke Mama, danke Papa.

And finally, I would like to sincerely thank Henri for all the love, hugs and chocolate whenever I needed it the most.

Espoo, November 19, 2018

Rebecca Heilmann

Contents

Chapter 1

Introduction

Nanoparticles provide various interesting and unique optical properties. One of these effects can be seen in stained glass windows: small metal particles mixed in the glass during the manufacturing process leads to coloured glass. Gold, for example, creates red and silver yellow stained glass [1]. These effects are studied in the field of plasmonics which combines the fields of photonics, electronics and nanotechnoloy. Metals provide collective oscillations of their conduction electrons, the so-called plasmons. In nanoparticles, a special type of plasmons, the localized surface plasmon resonances (LSPRs) can couple to light and form new optical modes [2]. The LSPRs exhibit a high degree of local field confinement and sensitivity to their local environment [3]. This leads to various applications of nanostructures such as optical imaging [4], biomedicine [5] and solar cells [6][2]. Metal nanoparticles, however, provide very high ohmic losses and heating [6][7]. Recently dielectric materials with a high refractive index became more and more popular for nanoscale applications due to their low-dissipative properties and their ability to not only enhance electric but also magnetic resonances [6][7][8][9].

Another very interesting phenomenon is the strong coupling. If two oscillating systems are coupled to each other they may form hybrid states of their original states. In the quantum domain the systems involved are an electromagnetic field and a two-level system, e.g. an emitter. If nanoparticles are arranged in arrays and interact with light they form the so-called surface lattice resonances. These resonances can then couple to emitters, namely dye molecules and even be in the strong coupling regime [10][11][12]. The strong coupling regime is connected to coherence phenomena [13] and is therefore linked to stimulated emission, gain and lasing [10]. Systems in the strong coupling regime have been reported to lase [14] and form Bose-Einstein condensates [15].

The aim of this Master's thesis is the fabrication of dielectric nanopar-

ticle arrays, namely germanium and amorphous silicon nanoarrays and the measurement of the dispersion of light through those arrays. Furthermore, the strong coupling between the SLRs of the nanoparticle arrays and dye molecules was studied. In addition to this, gold nanoparticle arrays have been fabricated and the same measurements were taken in order to compare the results between metallic and dielectric nanoparticle arrays.

The thesis is divided as following: Chapter 2 explains the phenomenon of strong coupling in detail and provides a quantum description of the strong coupling between a two-level system and a quantized field. Chapter 3 discusses the SLRs in nanoparticle arrays. Here, first plasmonic resonances will be explained followed by a more detailed discussion why it is of interest to switch from metallic to dielectric nanoarrays. Finally, a short qualitative description on how strong coupling between SLRs and dye molecules emerges is provided. In Chapter 4, the fabrication of the nanoarrays is explained followed by the description of the transmission measurement setup in Chapter 5. The results of the transmission measurements are presented in Chapter 6. First, the dispersions of the arrays without dye molecules are presented and the arrays of different materials are compared. Secondly, the dispersions of the arrays with dye molecules on top are presented. Indications of strong coupling between dye molecules and dielectric nanoparticle arrays have been observed. Chapter 7 gives a conclusion regarding the results obtained in this work as well as an outlook on future developments and improvements.

Chapter 2

Strong coupling

2.1 Phenomenological description of strong coupling

Coupled systems can be intuitively grasped by thinking of two pendula which are connected by a spring. If one pendulum is brought into oscillation, the other pendulum starts swinging, too. An exchange of energy takes place. The exact motion of the system is dependent on several factors such as the rigidity of the spring or the energy with which the first pendulum is oscillating. In the quantum mechanical description the energy is directly proportional to the frequency of oscillations. Therefore, energy and frequency are used as interchangable terms in the following. If the oscillation amplitudes of the pendula are small, the pendula can be described as harmonic oscillators. In general, if two harmonic oscillators are coupled they exchange energy such that new modes, i.e. energy states of the system, are obtained with different energies from those of the original modes, the energy spectrum of the system is modified. The difference between the original and modified modes depends on the strength of the coupling. In case this energy modification is large enough, i.e. significant compared to the original mode energies of the system and of the same order or larger than the damping, the system is in the strong coupling regime. The new modes in this strong coupling regime are now hybrids of the two original modes, i.e. new energy states are arising [10].

In quantum mechanics, the coupled system can consist, for instance of a light field and an atom instead of the two pendula in the classical picture. Here, the energy of the atom is constant and given by the difference between energy states of the atom. The energy of the light field, however, is tunable since the energy of the light changes with the frequency or wave vector. If one draws the energy dependence on the wave vector of light, i.e. the dispersion

relation, and also the constant energy of the atom, those energies will cross. This crossing is called resonance and describes the point at which the energies of the light and the atom are the same. These lines are depicted as the blue and yellow lines in Figure 2.1, respectively. If the light and the atom are now strongly coupled, the coupled modes are hybrids of the two original modes and the dispersion relation takes the form of hyperbolas, as depicted by the red lines in Figure 2.1. Far away from the resonance, the original oscillators and the coupled systems are practically the same, while near the resonance the new normal modes appear and the so called avoided crossing is observed. The energy difference between the upper and lower hyperbola is referred to as Rabi splitting. The strong coupling regime can be defined as the point from which on the Rabi splitting is experimentally visible, i.e. the splitting is larger than the linewidth, which is represented by the width of the energy line [10].

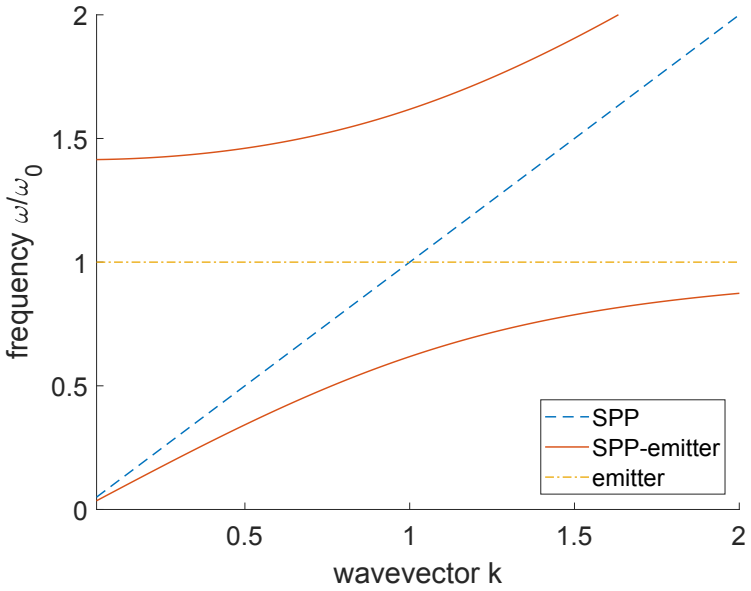

Figure 2.1: Strong coupling between an optical mode and an emitter. The solid red line corresponds to the dispersion of the coupled system. The horizontal yellow dash-dotted line depicts the emitter energy and the diagonal blue dashed line the dispersion of the optical mode. The x-axis decribes the in-plane wavevector k, the y-axis describes is the frequency ω normalized to ω_0.

2.2 Interaction between a quantum two-level system and a quantized field

Generally, a two-level system can be described with energies of an excited state E_e and of a ground state E_g with an energy difference $E_e - E_g = \hbar\omega_0$, where $\hbar$ is the reduced Planck constant and ω_0 the frequency related to that energy difference. If the two-level system or emitter is now interacting with an electromagnetic field, several things can happen. The quanta of the field, photons, can be absorbed by the system which transfers it from the ground to the excited state if the photons have the energy $\hbar\omega_0$. This energy corresponds to light of the wavelength $\lambda_0 = \frac{2\pi c}{\omega_0}$, where c is the speed of light. Additionally, the light field can induce emission where the system falls from the excited to the ground state releasing another photon of the energy $\hbar\omega_0$. This emitted photon has the same direction and polarization as the photon which is inducing the emission. This process is called stimulated emission. A third possibility is the spontaneous emission of a photon, with $\hbar\omega_0$ with arbitrary direction and polarization [16].

In the quantum description of the interaction between the two-level system and a quantized field, the emitter is described by an excited state $|e\rangle$ and a ground state $|g\rangle$. Transitions from the ground to the excited state are described by $\sigma_+ = |e\rangle\langle g|$ and from the excited to the ground state by $\sigma_- = |g\rangle\langle e|$. The matrix $\sigma_z = |e\rangle\langle e| - |g\rangle\langle g|$ provides the eigenstates [10]. The Hamiltonian which describes the energy in the whole system for a single emitter is:

$$\hat{H} = \hat{H}_0 + \hat{V}, \tag{2.1}$$

where

$$\hat{H}_0 = E_e |e\rangle\langle e| + E_g |g\rangle\langle g| \tag{2.2}$$

is the energy of the two-level system and

$$\hat{V} = -e\langle e|\hat{\mathbf{r}}|g\rangle \cdot \hat{\mathbf{E}}(\mathbf{R},t)|e\rangle\langle g| - e\langle g|\hat{\mathbf{r}}|e\rangle \cdot \hat{\mathbf{E}}(\mathbf{R},t)|g\rangle\langle e| \tag{2.3}$$

the interaction with the field $\hat{\mathbf{E}}(\mathbf{R},t)$ with e being the elementary charge. In the interaction picture this leads to a Hamiltonian of the form

$$\hat{V}_I = \hbar\left(g\hat{a}\hat{\sigma_+}e^{-i(\omega-\omega_0)t} + g^*\hat{a}^\dagger\hat{\sigma_-}e^{i(\omega-\omega_0)t}\right) + \hbar\left(g^*\hat{a}\hat{\sigma_-}e^{-i(\omega+\omega_0)t} + g\hat{a}^\dagger\hat{\sigma_+}e^{i(\omega+\omega_0)t}\right), \tag{2.4}$$

where ω_0 is the frequency of the emitter, $\hat{a}^\dagger$ is the creation, $\hat{a}$ the annihilation operator of the photon and g is the coupling constant. Within the so-called Rotating Wave Approximation, i.e. neglecting the counter-rotating terms

$\omega + \omega_0$, and changing back from the interaction picture, the Hamiltonian becomes:

$$H = \frac{1}{2}\hbar\omega_0\sigma_z + \hbar\omega\hat{a}^\dagger\hat{a} + \hbar(g\hat{a}\sigma_+ + h.c.).$$

This so-called Jaynes-Cummings Hamiltonian describes a quantized field interacting with a two-level system in general. This Hamiltonian only couples the states $|e\rangle|n\rangle$ and $|g\rangle|n+1\rangle$, where n refers to the photon number in that state. Since this means that only one photon is emitted/absorbed at a time when the atom makes a transition between the two states, the Hamiltonian can be written as:

$$H = \sum_n H_n. \tag{2.5}$$

In the vector basis $|e\rangle|n\rangle = \begin{pmatrix}1\\0\end{pmatrix}$ and the ground state $|g\rangle|n+1\rangle = \begin{pmatrix}0\\1\end{pmatrix}$ the Hamiltonian H_n becomes:

$$H_n = \hbar\left(n+\frac{1}{2}\right)\omega\begin{pmatrix}1&0\\0&1\end{pmatrix} - \frac{\hbar}{2}\begin{pmatrix}-\delta & 2g\sqrt{n+1}\\ 2g\sqrt{n+1} & \delta\end{pmatrix}, \tag{2.6}$$

where $\delta = \omega - \omega_0$, the so called detuning. The eigenvalues can be obtained by diagonalizing and they become:

$$E_{1n} = \hbar\left(n+\frac{1}{2}\right)\omega - \frac{1}{2}\hbar\sqrt{\delta^2 + 4g^2(n+1)} \tag{2.7}$$

$$E_{2n} = \hbar\left(n+\frac{1}{2}\right)\omega + \frac{1}{2}\hbar\sqrt{\delta^2 + 4g^2(n+1)}. \tag{2.8}$$

The generalized Rabi frequency can be defined as

$$\mathcal{R}_n = \sqrt{\delta^2 + 4g^2(n+1)} \tag{2.9}$$

and the eigenstates become

$$|1n\rangle = -\sin\theta_n|e\rangle|n\rangle + \cos\theta_n|g\rangle|n+1\rangle \tag{2.10}$$

$$|2n\rangle = \cos\theta_n|e\rangle|n\rangle + \sin\theta_n|g\rangle|n+1\rangle, \tag{2.11}$$

with

$$\cos\theta_n = \frac{\mathcal{R}_n - \delta}{\sqrt{(\mathcal{R}_n-\delta)^2 + 4g^2(n+1)}} \tag{2.12}$$

$$\sin\theta_n = \frac{2g\sqrt{n+1}}{\sqrt{(\mathcal{R}_n-\delta)^2 + 4g^2(n+1)}}. \tag{2.13}$$

On resonance, when $\delta = 0$ which means that the field and transition energy are the same it follows

$$|1n\rangle = \frac{1}{\sqrt{2}} \left[- |e\rangle |n\rangle + |g\rangle |n+1\rangle \right] \tag{2.14}$$

$$|2n\rangle = \frac{1}{\sqrt{2}} \left[|e\rangle |n\rangle + |g\rangle |n+1\rangle \right] \tag{2.15}$$

$$E_{1n} = \hbar \left(n + \frac{1}{2} \right) \omega - \hbar g \sqrt{n+1} \tag{2.16}$$

$$E_{2n} = \hbar \left(n + \frac{1}{2} \right) \omega + \hbar g \sqrt{n+1}. \tag{2.17}$$

One can see that the eigenstates of this system are an equal superposition of the ground state with an extra photon and the excited state without an extra photon. The split between the modes is $\Delta E = 2\hbar g\sqrt{n+1}$. Due to the $n+1$ term, there is also a splitting for $n = 0$ which is referred to as the vacuum Rabi splitting. The discrete set of states with splittings for $n \in \mathbb{N}_0$ is the so called Jaynes Cummings ladder [11][10].

Usually, there are many emitters involved in the interaction. Therefore, it is useful to expand the fully quantum mechanical description to a many-emitter case with N two-level systems. The Hamiltonian then becomes

$$H = \frac{1}{2}\hbar\omega_0 \hat{S}_z + \hbar\omega \hat{a}^\dagger \hat{a} + \hbar \left(g \hat{a} \hat{S}_+ + h.c. \right), \tag{2.18}$$

where $\hat{S}_z = \sum_{i=1}^{N} \sigma_z^{(i)}$ and $\hat{S}_+ = \sum_{i=1}^{N} \sigma_+^{(i)}$ are collective two-level operators. This Hamiltonian is referred to as Dicke Hamiltonian. It is sufficient to assume that the number N of emitters is large but the number of excited emitters is small, such that the two-level system does not become saturated.

Using the Holstein-Primakoff transformation which transforms spin-systems or two-level atoms to bosonic systems leads to

$$\hat{S}_+ = \hat{b}^\dagger (N - \hat{b}^\dagger \hat{b})^{1/2}, \hat{S}_- = (N - \hat{b}^\dagger \hat{b})^{1/2} \hat{b}, \hat{S}_z = \hat{b}^\dagger \hat{b} - \frac{N}{2}, \tag{2.19}$$

where $\hat{b}$ and $\hat{b}^\dagger$ are bosonic operators. For large N, the spins can be approximated by $\sqrt{N}b$ and the Hamiltonian becomes [11][10]

$$\hat{H} \simeq \hbar\omega_0 \left(-\frac{N}{2} + \hat{b}^\dagger \hat{b} \right) + \hbar\omega \hat{a}^\dagger \hat{a} + \hbar g \sqrt{N} (\hat{a}^\dagger \hat{b} + h.c.). \tag{2.20}$$

This Hamiltonian acts as two coupled harmonic oscillators with bosonic modes $\hat{a}$ and $\hat{b}$. The collective two-level system modes sum up as a quantum

oscillator with the mode $\hat{b}$. The hybrid eigenmodes of this Hamiltonian can be solved and lead towards a splitting of the size $\Omega = 2g\sqrt{N}$, where the coupling coefficient is $g \propto d\sqrt{\omega_0/(V\hbar\epsilon_0)}$ and V is the mode volume. This leads to the following proportionality:

$$\Omega \propto d\sqrt{\frac{N}{V}} = d\sqrt{c}, \tag{2.21}$$

where c is the concentration. The splitting is proportional to the square root of the concentration and linearly proportional to the dipole moment. The eigenmodes of the system are hybrids of having a photon in the mode, i.e. the photon field, or an excitation in the giant oscillator mode which consists of N harmonic oscillators. This $\sqrt{c}$ dependence also demonstrates that the emitters are acting coherently [11][10].

Chapter 3

Optical resonances in nanoparticle arrays

3.1 Plasmons

Plasmons are a class of quasiparticles which are related to the electronic properties of a metal. A metal can be described to consist of two parts: 1) an array of positively charged ions which include the nuclei valence electrons and 2) the free electron gas which surrounds the ions and is negatively charged. These free electrons are weakly bound to the metal atoms and display a high mobility. Therefore, they govern the electrical conductivity of the metal. The first model to describe the electronic properties of metals by free electrons has been proposed by Drude in 1900, later modified by Lorentz (Drude-Lorentz model) and Sommerfeld (free electron or Drude-Sommerfeld model) [17]. If an electric field is applied around a piece of metal, one can imagine the free electrons to follow this field in order to cancel the field inside the metal causing the ions to be uncovered. If the electric field is now turned off, the electrons are attracted by the ions and move back. On the other hand the electrons also repel each other and an oscillation occurs. The frequency of this oscillation is the so-called plasma frequency ω_P and is defined as

$$\omega_P = \sqrt{\frac{ne^2}{m_e \epsilon_0}}, \tag{3.1}$$

where n is the electron density, e the elementary charge, m_e the electron mass and ϵ_0 the dielectric constant. The quanta of these oscillations are referred to as plasmons. The energy of the plasmons is accordingly

$$E_P = \hbar \omega_P, \tag{3.2}$$

where $\hbar$ is the reduced Planck constant [18].

3.1.1 Surface Plasmon Polaritons (SPPs)

Surface plasmons are plasmons located at a metal surface with a plasma frequency of $\omega_{SP} = \omega_P/2$ [19]. If an electromagnetic wave excites a plasmon near a plane metal surface, the resulting plasmonic wave is the quasiparticle called Surface Plasmon Polariton (SPP). The resonant modes which occur if the external light field matches the surface plasmon frequency and wave vector are called Surface Plasmon Resonances (SPRs). Figure 3.1 shows the dispersion relation of SPPs on a metal surface as well as the dispersion relation of light. The SPP dispersion is always below the dispersion of the light line, i.e. the dispersion of light propagating in free space, and therefore SPPs can neither radiate to far-field or to freely propagating light [19].

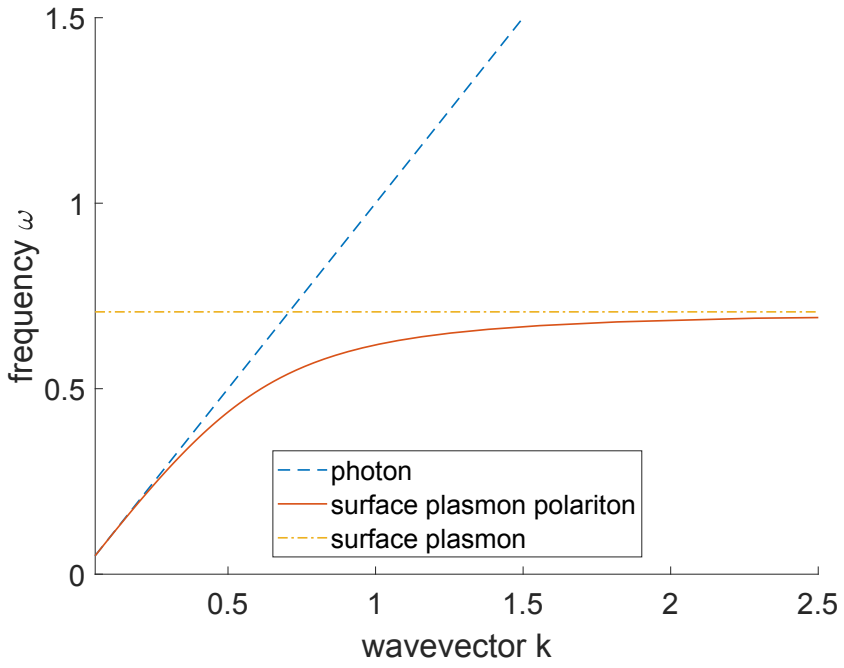

Figure 3.1: Dispersion of SPPs on a metal surface. The dashed line represents the dispersion relation of light, the dashed dotted line is ω_{SP}, i.e. the surface plasma frequency, and the solid line is the dispersion of the surface plasmon polariton.

The coupling between light and SPPs can, however, be achieved by mode coupling. This can be done e.g. by prism coupling according to the Otto configuration or the Kretschmann-Raether scheme.

Both methods make use of attenuated total reflection. In the Kretschmann-Rather scheme a dielectric prism is located on a metal film. Light is illuminat-

ing the metal film through the prism at an angle larger than the angle of total internal reflection. Since the prism is optically denser than the surrounding air, the wavevector of light is increased in it and at a certain incidence angle the wavevector in the prism matches the SPP wavevector. The total internal reflection leads towards an evanescent wave which couples to the SPP [19]. Another possibility is grating coupling where a grating is created on an otherwise smooth metal surface. The incoming wave is diffracted at the structures and some diffracted components will have a wavevector matching to the SPP wavevector and can therefore couple to the SPPs [19].

The SPP field is concentrated to a metal surface and is therefore noticeably enhanced but decays exponentially perpendicular to the surface, i.e. it is evanescent [19].

3.1.2 Localized Surface Plasmon Resonances (LSPRs)

In other metallic geometries than plane surfaces such as particles, coupling between the surface plasmons and light leads towards other types of excitations that are called Localized Surface Plasmon Resonances (LSPRs). LSPRs are fundamentally different from SPPs, since their resonances are characterized by the size and shape of the particles. These frequencies can be modified by changing the size and the shape of the metallic particle as well as its dielectric constant. Furthermore, the LSPRs are confined to metallic objects in contrast to SPPs that propagate. LSPRs can be, unlike SPPs, excited by freely propagating light [19].

In case of well separated nanoparticles with a diameter much smaller than the wavelength of the external light field, the absorption spectrum shows a broad and intense peak often in the visible spectrum. The exact position, sharpness and peak height is dependent on the size, the shape, the material and the surrounding material of the particle [20]. Those nanoparticles can also act as nano antennae , i.e. convert electromagnetic radiation into localized energy and vice versa [21]. Generally, an antenna is of the characteristic length

$$L = \frac{\lambda}{2}, \tag{3.3}$$

where λ is the wavelength of the ingoing radiation. Hence, λ corresponds to the resonant wavelength. Since incident light of optical frequencies are not reflected perfectly from the surfaces of metals, optical antennae are resonant to an effective wavelength λ_{eff} which is shorter than λ. The effective wavelength can be scaled as

$$\lambda_{eff} = a + b\frac{\lambda}{\lambda_P}, \tag{3.4}$$

where a, b are coefficients that are dependent on the shape and size of the antenna and λ_P the plasma wavelength corresponding to the plasma frequency ω_P [21]. The coefficients a and b follow, however, complex calculations. Combining this with Equation 3.3 gives

$$\lambda = \frac{\lambda_P}{b}(2L - a) \tag{3.5}$$

for the resonant wavelength λ. Typical values for λ_P are 138 nm and 135 nm for Au and Ag, respectively. For a gold nano rod of a diameter of 5 nm and a length of 110 nm, $\lambda_{eff} = \lambda/5.3$ and hence $L = \lambda/10.6$. The wavelength at the resonance of this particular rod is then $\lambda = 1166$ nm [21]. If the particles are ordered in arrays, the particles interact with each other and the optical response changes. Such arrays lead to sharp peaks in the transmission [19] and will be discussed next.

3.2 Surface Lattice Resonances (SLRs)

If metallic nanoparticles are arranged in lattice patterns, new optical modes are arising. These optical modes are called Surface Lattice Resonances (SLRs) and are combinations of the LSPRs of the single nanoparticles and the Diffracted Orders (DOs) caused by the periodic structures [12][22]. It is important to note that the spacing between the particles has to be of the order of the wavelengths of the light in the dielectric media surrounding the particle array. Since the periodicity is similar to the wavelength of the light, diffraction plays an important role in the SLRs [11]. In the following, a model to describe the SLRs will be introduced. First, the dispersion of light through a lattice will be described and then refined by describing the nanoparticles as point dipoles.

3.2.1 Empty lattice approximation

The dispersion relation of light in a homogeneous medium is:

$$k = \frac{nE}{\hbar c}, \tag{3.6}$$

where k is the wavevector, E the energy of the photons and n the refractive index of the surrounding medium, $\hbar$ the reduced Planack constant and c the speed of light. If one restricts the space formed by k_x, k_y and E, the propagating plane waves with the wave vector $\vec{k} = (k_x, k_y, k_z)$ form a cone with the edges $k_x^2 + k_y^2 = (nE)^2/(\hbar c)^2$. Outside this cone the modes become

evanescent, i.e. they decay exponentially, and since the optical modes in the plane are of main interest, one can also only consider the modes with $k_z = 0$ so that only the surface of the cone is left [11].

If one now assumes to have a lattice of infinite length with periodicities p_x and p_y in the x- and y-direction, respectively, all solutions to the wave equation are also periodic while the phase difference at the unit cell boundaries is fixed. The phase difference comes from the in-plane wave vector of the modes. The modes with the in-plane wave vector differing by an integer multiple of the reciprocal lattice vectors ($\vec{G}_x = 2\pi/p_x\hat{x}$ and $\vec{G}_y = 2\pi/p_y\hat{y}$) are equivalent. This leads to multiple cones which are reproduced at the origin of the reciprocal lattice vectors as shown in Figure 3.2 [11].

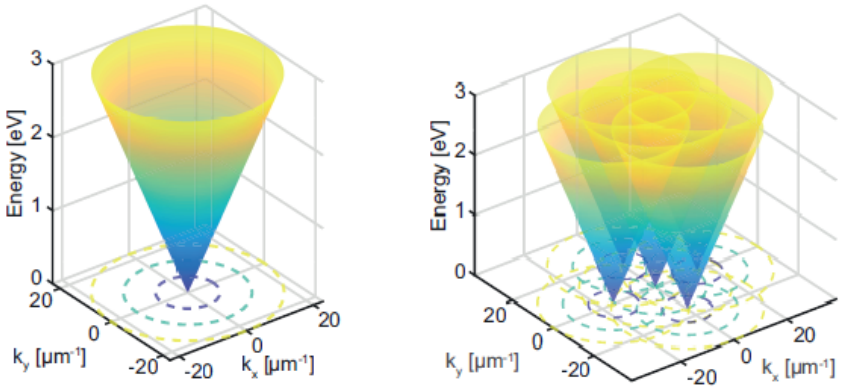

Figure 3.2: Left: Dispersion of light in k_x, k_y and E-space for $n = 1.5$. On the surface of the cone are the modes that can propagate in the (x, y)-plane. Right: Dispersion of light in a square lattice geometry in k_x, k_y and E-space with $n = 1.5$ and periodicities of 400 nm in x and y-direction. The four extra cones resemble the first order DOs. Taken from [11].

3.2.2 Lattice of Point Dipoles

Now that the dispersion of light in a lattice geometry is described, we consider nanoparticles arranged in a lattice geometry and will see how the dispersion of light is affected. Small nanoparticles can be considered as individual point dipoles and can be added to the periodic system as scatterers. Let us consider that they are driven by light polarized linearly along the x-direction of the lattice. Because the dipoles will not radiate in the direction defined by the driving field, the effect of the periodicity in the x-direction is negligible. In

case the distance between the dipoles is large enough, the particles will not interact with each other and higher-order multipoles induced by near-field coupling between the particles are neglegible. Furthermore, only periodicities of λ/n are taken into into account. The light cones intersect in two directions which show quantitatively different behaviour as shown in Figure 3.3a. For incident light in the $k_y = 0$ plane, one receives the transverse magnetic modes (TM) which have the dispersion relation $E = \pm\frac{\hbar c}{n}(k_x^2 + G_y^2)^{1/2}$, where $\vec{G}_y = 2\pi/p_y$ is the lattice momentum. The lattice momentum is perpendicular to the in-plane wave vector of the incident light and gives a square root dependence on the total wave vector. If k_x is much smaller than G_y, the dispersion of the TM mode is approximately quadratic (see Figure 3.3b). The other type of dispersion are the transverse electric modes (TE) which are on the $k_x = 0$ plane. They have a linear dispersion $E = \frac{\hbar c}{n}(k_y \pm G_y)$ as the lattice momentum is in the same direction as the in-plane vector of the incident field (see Figure 3.3c). TM and TE modes are identical at the Γ-point, where $k_x = k_y = 0$ [11].

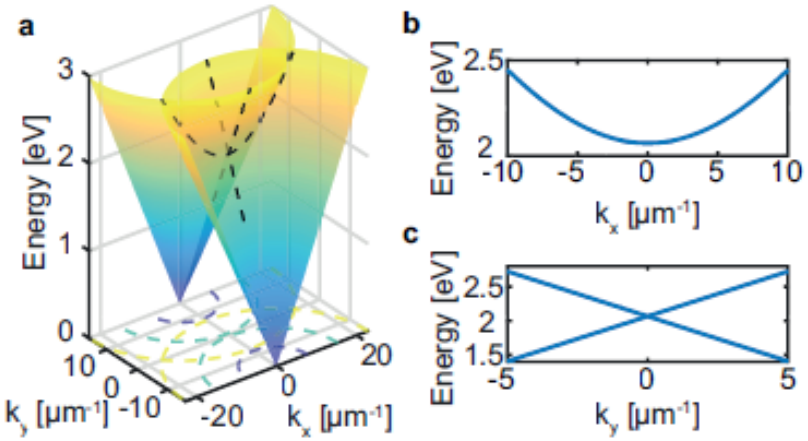

Figure 3.3: Dispersion of light in k_x, k_y and E-space for $n = 1.5$. (a) shows the intersection of uncoupled light cones. The TM modes ($k_y = 0$) and TE modes ($k_x = 0$) are shown in (b) and (c), respectively. The point at which the TM and TE modes cross is referred to as Γ-point. Taken from [11].

At the Γ-point, however, the optical modes which are propagating along the different directions can couple due to the scattering nature of the nanoparticle. Two hybrid modes, symmetric and asymmetric are formed and a small photonic bandgap arises (see Figure 3.4). The antisymmetric mode is dark,

or sub-radiant, and corresponds to a quadrupole excitation in the nanoparticle [11] [23].

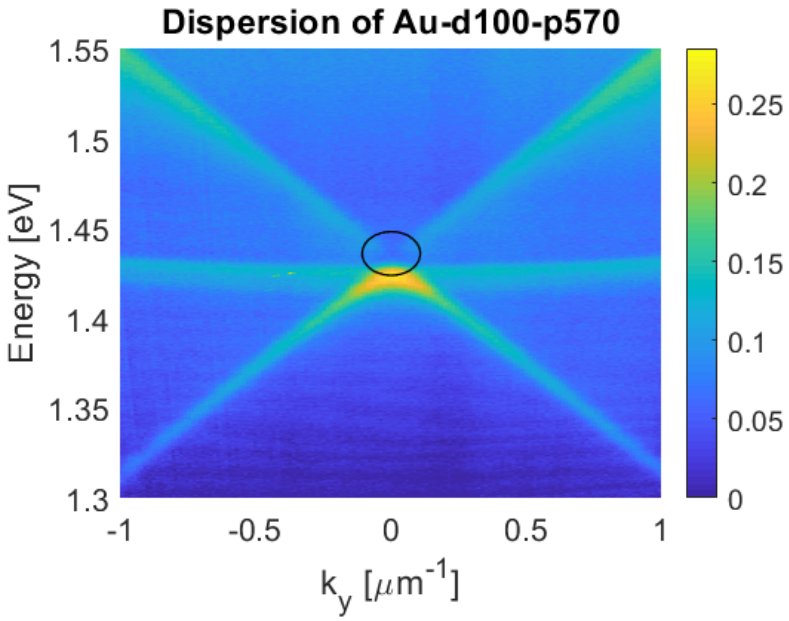

Figure 3.4: Measured SLR dispersion relation of a typical sample with clearly visible TE and TM modes. The dark mode is depicted by the black circle. k_y indicates the in-plane k-direction, i.e. the angle of incidence, in which the dispersion is measured. The used sample was an Au sample of cylindrical nanoparticles with a diameter of 100 nm and height of 50 nm separated by a periodicity of 570 nm in x- and y-direction.

Recapitulatory, in case of nanoparticle arrays, the LSPRs are given by the size and shape of the nanoparticle and the DOs by the lattice periodicity. By changing the lattice spacing it is possible to vary the location of the SLR, e.g. for larger periodicities the Γ-point lies at lower energies and for smaller periodicities at higher energies. The dispersion relation therefore undergoes a redshift for increasing periodicities. The position of the Γ-point in a lattice-like array with the periodicity $p_x = p_y = p$ can be estimated to be

$$E = \frac{\hbar c}{np}, \tag{3.7}$$

where $\hbar$ is the Planck constant, c the vacuum speed of light and n the refractive index of the medium the light propagates in [11].

3.3 From metals to dielectrics

The discussed features in the dispersion of nanoparticle arrays have been frequently studied for metals such as gold [3][24] and silver [25]. But why is it of interest to switch from metals to dielectrics?

In general, if light is scattered by spherical particles with a diameter on the order of the wavelength of the incoming light, the scattering process can be described by Mie theory. According to this, both metallic and dielectric materials can have strong scattering resonances. The scattering properties of lossless materials only depend on two parameters: the dielectric permittivity ϵ and a size parameter $q = 2\pi R/\lambda$ with the particle radius R and the wavelength of light λ. It is worth noting that the dielectric constant $\epsilon = \epsilon' + i\epsilon''$ defines the material response to any electric excitation and is frequency dependent. Here, the real part ϵ' describes the degree of metal polarization induced by the external electrical field and the imaginary part ϵ'' the phase shift of this polarization as well as losses [17]. In case of a fixed q, the only difference between metallic and dielectric materials is in ϵ.

Akimov *et al.* investigated the enhancement of nanoparticles of different materials in solar cell performance and found that dielectric nanoparticles can lead to similar or even higher enhancements than metal nanoparticles [6]. The scattering and absorbance cross-sections of a spherical particle with a diameter smaller than the wavelength λ of the incident light can be described as

$$\sigma_{scat} = \frac{1}{6\pi}\left(\frac{2\pi}{\lambda}\right)^4 |\alpha|^2 \tag{3.8}$$

and

$$\sigma_{abs} = \frac{2\pi}{\lambda}\,\mathrm{Im}(\alpha) \tag{3.9}$$

with

$$\alpha = 4\pi R^3 \frac{\epsilon - 1}{\epsilon + 2}, \tag{3.10}$$

where α is the polarizability of the particle [6]. This means that the scattering efficiency, i.e. the ratio of the scattering cross-section σ_{scat} and geometrical cross-section, of a nanoparticle is generally higher for a higher absolute value of σ, in case it is not in the range (-2;1). In addition, a negative ϵ always leads to a higher polarizability than a positive ϵ. At this point, it is important to note that metals always have a negative ϵ and dielectrics a positive ϵ for visible light. A larger scattering cross-section σ_{scat} means that very efficient scattering of light is provided by the nanoparticle and is desirable, considering that we are interested in the dispersion in nanoparticle arrays. In addition, the imaginary part of ϵ is connected to dissipation in the material

and the higher the dissipation, the higher the absorption. Generally, metals have very high absorption at the surface plasmon resonances which increases the overall performance of metal nanoparticles [26]. Dielectric nanoparticles, however, are low-loss materials and provide less absorption [7]. The dielectric functions of silicon and germanium are shown in Figures 3.5a and 3.5b, respectively. Figure 3.5c shows the dielectric function of gold. The visible spectrum corresponds to energies between 1.6 eV (red light) and 3.2 eV (violet light). If one compares the values for ϵ', the absolute value for Au is higher than for Si or Ge. The imaginary part ϵ'', however, is smaller for Si and about the same for Ge compared to Au. It is, e.g. for 1.6 eV 0.057 for Si, 3.77 for Ge [27] and about 3 for Au [28].

Figure 3.6 shows the enhancements of nanoparticles of different materials in solar cell performance for existing materials with a complex ϵ (stars) and the ideal material with zero dissipation, i.e. only a real ϵ (solid black line). It is obvious that the enhancement of the metal nanoparticles is much lower than the enhancement of the ideal material, while the enhancement of the dielectric nanoparticles is much closer to the enhancement of the ideal material [6]. Therefore, many plasmonic effects observed in metallic materials can be realized with high-index dielectric materials. Generally, group IV and group III-V semiconductors with refractive indices above 2 might show strong scattering resonances in the visible and near infrared spectrum such as germanium, silicon and GaAs. Electric and magnetic dipole resonances at visible wavelengths have been reported for spherical Si nanoparticles [7] and will be discussed next.

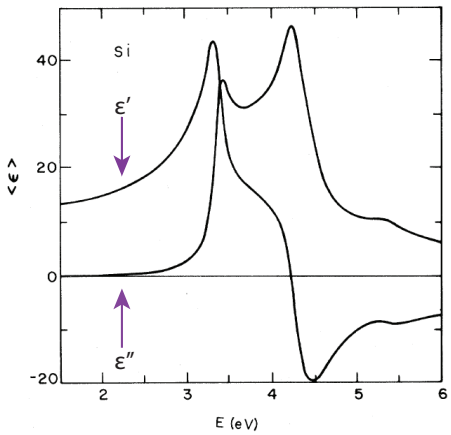

(a) Dielectric function of silicon. Taken from [27].

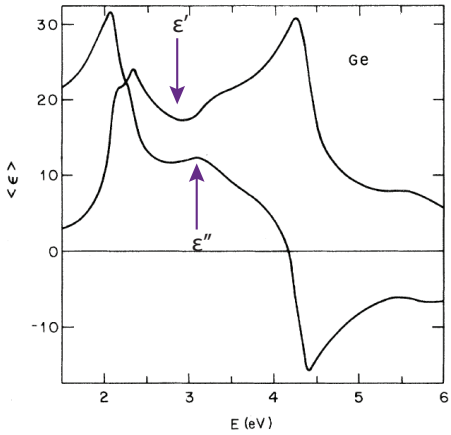

(b) Dielectric funtion of germanium. Taken from [27].

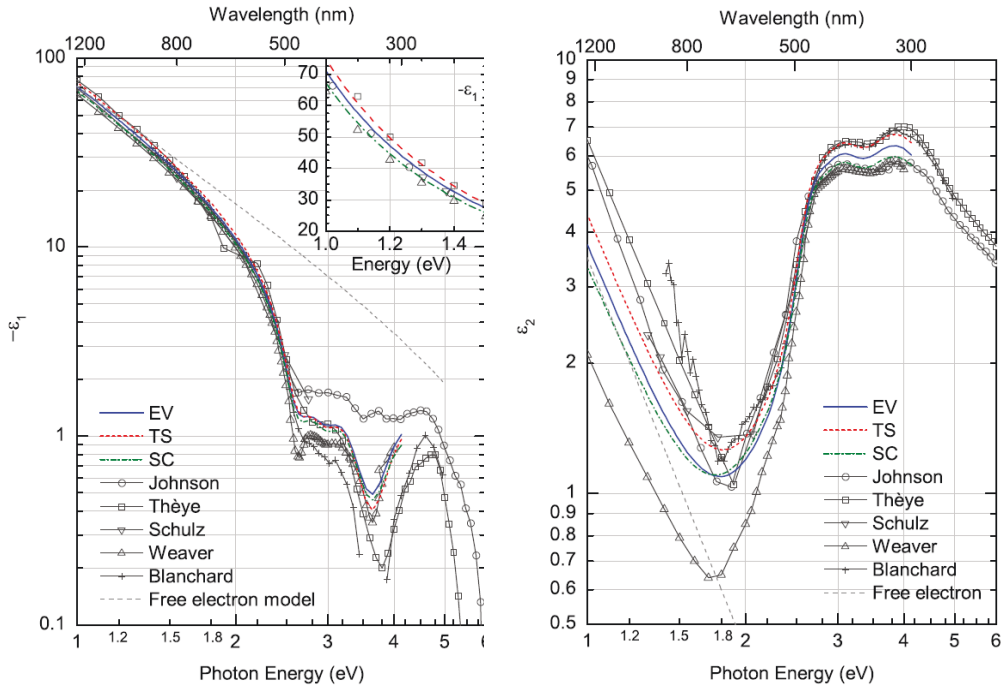

(c) Dielectric function of gold, real and imaginary part left and right, respectively. Taken from [28].

Figure 3.5: Dielectric functions of (a) Si, (b) Ge and (c) Au.

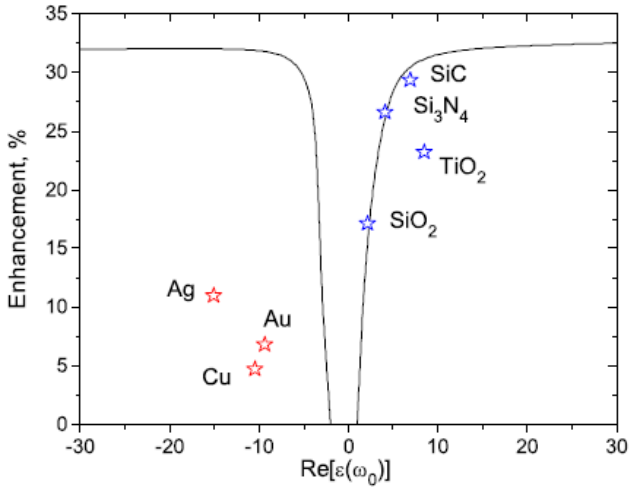

Figure 3.6: Enhancements of nanoparticles of different materials in solar cell performance. Existing materials are depicted by red stars (metals) and blue stars (dielectrics). The black solid line represents the dependence of the enhancement of an ideal material (zero dissipation, i.e. only real ϵ) on ϵ. Taken from [6].

3.4 Magnetic resonances in dielectric nanoparticle arrays

Besides their ability to enhance the efficiency of the nanoparticle resonances dielectrics also provide many other interesting features. In the case of spherical nanoparticles, metal particles only produce electric localized surface plasmon resonances while the magnetic response remains negligible due to a vanishing field inside the sphere. In dielectric materials, both magnetic and electric responses can be observed. Due to a coupling of incoming light to the circular displacement currents of the electric field, the magnetic resonances occur. This happens when the size of the particle is comparable to the wavelength inside of the particle $2R = \lambda/n$, with n the refractive index [7].

In a spherical nanoparticle with coinciding electric (a_1) and magnetic (b_1) multipole coefficients ($a_1 = b_1$) backward scattering vanishes due to destructive interference in the backward direction. This is known as the first Kerker condition according to which zero-backscattering occurs if a particle has similar electric and magnetic properties ($\epsilon = \mu$) and has been realized experimentally [29] [30].

Optically induced resonances can be achieved in dielectric nanoparticles not only for spheres but for spheroids, disks, rings and cylinders. Changing geometric parameters of the nanoparticles leads to the ability to tune the spectral positions of electric and magnetic dipole resonances. Figure 3.7 shows the dark-field optical microscope images (top left), SEM images (top right) and dark-field scattering spectra (bottom) of spherical Si nanoparticles with diameters of approximately 100 nm (A), 140 nm (B) and 180 nm (C). It is obvious that with increasing diameter the magnetic dipole (md) resonances shift to longer wavelengths and electric dipole (ed) and magnetic quadrupole (mq) resonances occur [7].

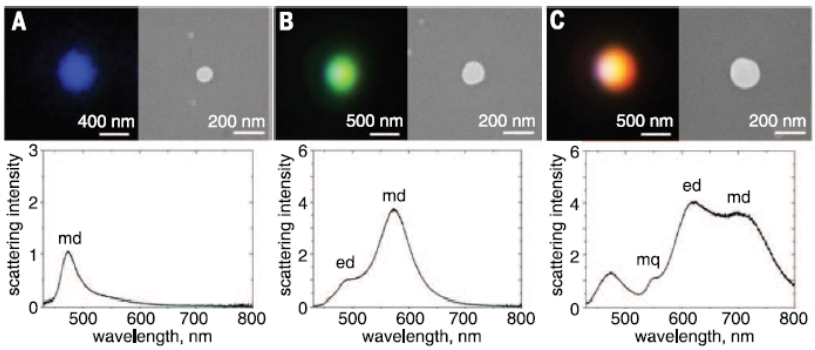

Figure 3.7: A, B and C show the dark-field optical microscope images (top left), SEM images (top right) and dark-field scattering spectra (bottom) of spherical Si nanoparticles with diameters of approximately 100 nm (A), 140 nm (B) and 180 nm (C). md, ed and mq are the magnetic dipole, electric dipole and magnetic quadrupole resonances, respectively. Taken from [7].

Single particle resonances as well as extinction cross sections of nanoparticle arrays, e.g. consisting of silicon, have been investigated in the literature. Evlyukhin *et al.* found that the optical response features are analogous to the LSPRs and DOs described in Section 3.2 [9]. Several works have showed that it is possible to tune the electromagnetic dipole resonances by the far-field diffraction coupling of electric and magnetic dipole resonances. Periodic arrays consisting of cylinders made out of amorphous silicon were studied by systematically changing the periodicity in either x- or y-direction while keeping the other one constant [31]. With increasing periodicity in x-direction, the magnetic dipole resonance undergoes a redshift and similarly the electric dipole resonance undergoes a redshift when the periodicity in y-direction is changed if the array is illuminated by light polarized along the x-direction. Additionally, the linewidths of the redshifting resonances become narrower [8].

3.5 SLRs at strong coupling regime with dye molecules

Now that we know how the surface lattice resonances in nanoparticle arrays in theory look like we will consider how to achieve strong coupling within the SLRs.

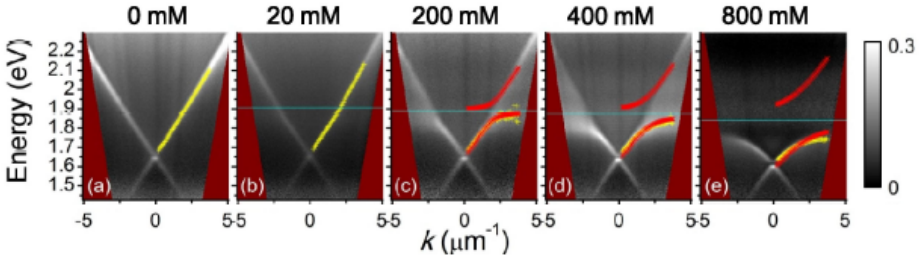

Figure 3.8: Dispersion of a silver nanoparticle array with increasing DiD concentration from 0 mM over 20 mM, 200 mM, 400 mM to 800 mM. The absorption peak of the DiD molecules is depicted as horizontal blue line. The avoided crossings are clearly visible for increasing DiD concentration. Taken from [13].

To recap what was already described in Chapter 2, the strong coupling regime is defined as the point at which the avoided crossing can be observed. It is possible to achieve strong coupling between the SLR modes and the excitation transition of emitters, i.e. dye molecules, as shown for the first time by Väkeväinen *et al.* in [12]. The dye molecules should have an absorption peak in the same frequency range as the SLR modes. Figure 3.8 shows what the dispersion relation of a silver nanoparticle array with DiD dye molecules of different concentrations on top looks like [13]. With increasing concentration the branches of the TE modes start to bend and the avoided crossing becomes visible. The size of the avoided crossing is square-root dependent on the molecular concentration of the dye molecules as expected theoretically (see Figure 3.8 and Equation 2.21) [13].

Having covered the theoretical part of understanding the dispersion of nanoparticle arrays and the strong coupling between their SLRs and dye molecules in Chapter 4 the fabrication of metal and dielectric nanoparticle array samples will be described.

Chapter 4

Sample fabrication

In this chapter the fabrication process of nanoparticle arrays of three different materials, namely gold, germanium and amorphous silicon, will be explained. While the fabrication process used to fabricate Au and Ge nanoarrays is already well established in our group, the fabrication process of the a-Si nanoarrays required a new additional step, the so-called reactive ion etching. This turned out to be a rather tedious task which will be seen in Section 4.2.1. After that, the preparation of the dye molecules which are used in order to achieve strong coupling, is introduced.

4.1 Gold and germanium nanoarrays

The gold and germanium nanoarrays are produced following the same procedure. All samples were prepared on a 20 mm x 75.6 mm x 1mm glass substrate. First, 350 μL of PMMA A4 was spin coated on the substrates at 3000 RPM for 60 seconds and then baked at 175 °C for two minutes to remove any excess solvent. Then, 10 nm of aluminum was evaporated on top of the PMMA layer to obtain conductivity for electron beam exposure. With electron beam lithography, nanoparticle array layouts, prepared beforehand using MATLAB, were patterned into the resist. After this, the aluminum layer was etched in AZ 351 B for a minute and immersed in DI-water for 30 seconds. After etching, the PMMA was developed in IPA:MIBK (1:3) for 15 seconds, followed by immersion into IPA for 30 seconds. After developing, 2 nm of titanium were evaporated followed by evaporation of the nanoparticle material with desired thickness (50 nm for gold and 100 nm for germanium). The titanium layer is necessary to enhance the adhesion between Au/Ge and the substrate to make sure that the particles stay on the substrate when different dyes are spin coated on the sample [12]. Additionally, one Ge sam-

ple was fabricated without the Ti layer to measure the pure Ge nanoparticle array dispersions. The final step was the lift off of the excess material so that only the nanoparticles were left on the substrates. For this, the samples were immersed in acetone for several hours. The individual fabrication steps are depicted in Figure 4.1. Each array consisted of 200 x 200 particles. Specifications can be found in Table 4.1

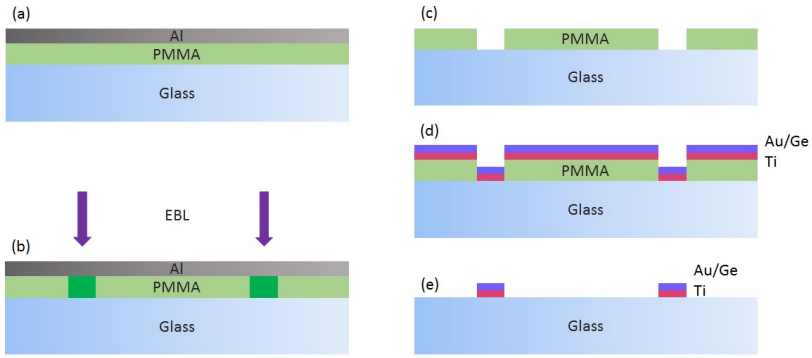

Figure 4.1: Schematic of the fabrication of Au and Ge nanoarrays. First, layers of PMMA and Al are applied onto the glass substrate (a) and exposed with EBL (b). After the Al etch and PMMA development, the EBL exposed locations are holes (c). 2 nm of Ti, followed by the nanoparticle material (Au and Ge) was evaporated on top of the sample (d). Finally, to remove the layers on the remaining PMMA, the sample was immersed in acetone. After the lift-off, only the nanoparticles were left on the substrate (e).

Sample	material	particle diameter [nm]	particle height [nm]	periodicity [nm]
#1	Au (Ti)	100 - 200	50 (2)	550 - 610
#2	Ge	100 - 300	100	560 - 610
#3	Ge (Ti)	100 - 300	100 (2)	550 - 580
#4	a-Si	150	100	500 - 610

Table 4.1: Specifications of the samples fabricated.

4.2 Amorphous silicon nanoarrays

In order to fabricate the amorphous silicon nanoarrays, a layer of 100 nm of amorphous silicon was deposited on a 20 mm x 75.6 mm x 1mm glass substrate with chemical vapor deposition. As a second step, chromium nanoar-

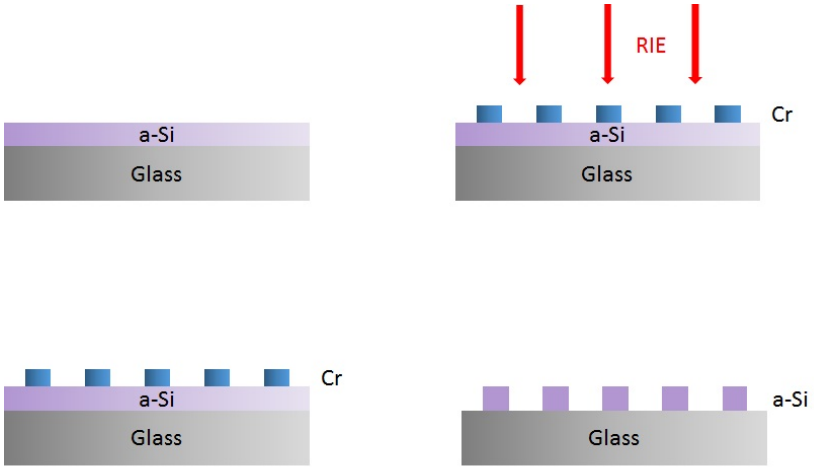

Figure 4.2: Schematic of he fabrication of the a-Si nanoarrays

rays were fabricated on top of the amorphous silicon similarly to the fabrication of the gold and germanium nanoparticles described in Section 4.1. In order to pattern the nanoarrays into the a-Si layer, the samples were now etched via reactive-ion-etching (RIE) while the chromium nanoparticles acted as a mask for the RIE. After this, the Cr was etched such that only the a-Si nanoparticles were left on the substrate. Each array consisted of 200 x 200 particles. Specifications can be found in Table 4.1. The RIE process will be discussed in more detail in the next section.

4.2.1 Reactive ion etching (RIE)

Since the etching of the a-Si through the Cr masks is the fabrication step which requires the most fine tuning, a short description of the reactive ion etching process is given in the following.

A RIE reactor is depicted in Figure 4.3. A gas is fed in between two parallel electrodes to which a radio frequency (RF) is applied, while the chamber pressure is held constant. The RF leads to ionization of the gas and this plasma is used for the etching process. In the vicinity of the lower electrode, the so-called sheath layer, a negative voltage is concentrated. If the ions enter this vicinity, they are accelerated proportional to the negative potential of the lower electrode and ion charge. They build up a kinetic energy and lose it when they hit the lower electrode. If now a sample is placed on the lower electrode, it is etched by the ions [32]. Here, both physical and chemical processes take part. Which process dominates can be determined by the choice of the feed gas, the pressure and the RF power. The different processes

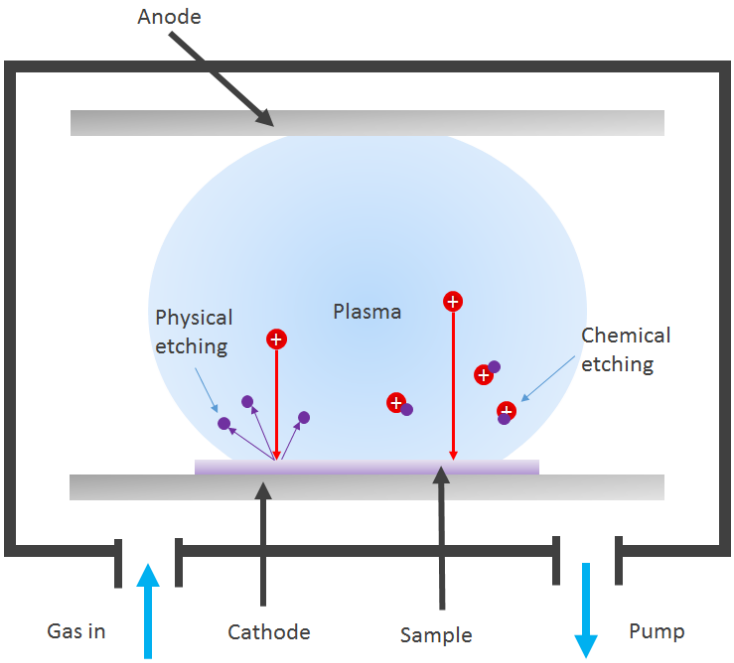

Figure 4.3: Schematic of the RIE reactor

can be divided into four groups: a) sputtering - removal of the substrate material by energetic ions, purely physical; b) chemical plasma etching - volatile species as a product of the reaction of neutral radicals formed in the plasma and substrate material; c) ion-enhanced chemical etching - damage of the substrate surface by energetic ions enhance its reactivity; d) inhibitor-controlled chemical etching - inhibitor layers from surfaces are removed by ions orthogonal to the ion flux. The RIE process leads to the ion-enhanced chemical etching and inhibitor-controlled chemical etching [33].

In order to transfer the mask pattern into the a-Si layer, an anisotropic etching process is necessary. Silicon is usually etched in a fluorine-based chemistry with SF_6 as main etchant creating SiF_4 as a volatile product. SF_6, however etches isotropically, i.e. equally etching rates in all directions. Therefore, a second gas is needed to passivate the etching process at the side walls. Here, CHF_3 has proven to be a good choice, since it forms polymers with the Si on the side walls and therefore adds a protective layer [32][34][33].

Now, there are five degrees of freedom in the RIE process: The RF power, the pressure, the two gas flows and the etching time. Generally one can note that a higher RF power and a lower pressure lead towards a higher anisotropy [32]. The five parameters were varied systematically in order to find the values which lead to the most anisotropic etching. To monitor how

the changes in the parameters affect the outcome of the etching process, i.e. the anisotropy, the samples were inspected with the SEM after each variation. Since the SEM requires a conductive surface, these samples were fabricated on 20 mm x 20 mm indium tin oxide (ITO)-covered glass slips. An ITO-cover provides a transparent conductive surface, which makes it possible to inspect structures on top of it with the SEM.

Starting point was the process introduced by Kravchenko *et al.* with a pressure of 30 mTorr, SF_6 flow of 80 sccm, CHF_3 flow of 30 sccm and an RF power of 10 W [34]. The etching time was 5 minutes. The first step was to increase the RF power to 30 W. Based on this, the CHF_3 flow has been gradually increased. The effect of increased CHF_3 can be seen in Figure 4.4. Figure 4.4e shows a failed etch, where the etching was too isotropic and hence underetched the mask. With increasing CHF_3 flow, the anisotropy increased as well and smaller structures became visible. At this point it became clear that with the available standard RIE reactor, we would not be able to achieve totally anisotropic etching. Ideally, one would achieve cylindrical nanoparticles but the resulting particles were cone-shaped, as can be seen from Figure 4.4.

Since in works by Yih *et al.* and Karouta *et al.* it is proposed that generally a higher RF power and a lower chamber pressure lead to higher anisotropies, the RF power and chamber pressure were investigated next [33] [32]. First, the chamber pressure was decreased gradually with the result that the smaller structures which became visible due to the increase of the CHF_3 flow were destroyed. Hence, it can be assumed that the anisotropy decreased by decreasing chamber pressure. Secondly, the RF power was increased, with the same result as decreasing chamber pressure: the anisotropy decreased.

Another property which has to be considered is the area of the material which is to be etched. Generally, a larger area means longer etching times [32] but can also enhance effects such as the so-called microloading [35]. This means that structures in the vicinity of large etching areas are etched faster than those in masked areas. This can lead to two possible outcomes: The structures close to the large etching areas are etched nicely while the ones in masked areas are not etched completely or that the ones in masked areas are etched nicely while the ones close to the large etching areas are etched too long which leads to an underetch of the structures. To investigate this, the arrays were produced on larger ITO-coated substrates which have the same size (20 mm x 75 mm) as the glass substrates used in the transmission experiments later on. After the first five minutes of etching, there were still residues of the a-Si visible and sample was put back into the reactor and etched for another minute. After this step, there was still a-Si visible and after another 30 seconds of etching time, there were no residues visible. The

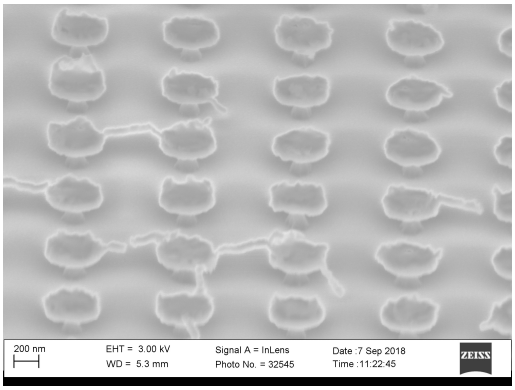

(a) CHF_3 flow of 40 sccm, mask size 400 nm.

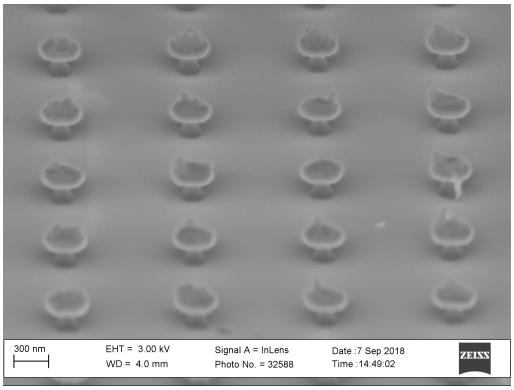

(b) CHF_3 flow of 50 sccm, mask size 300 nm.

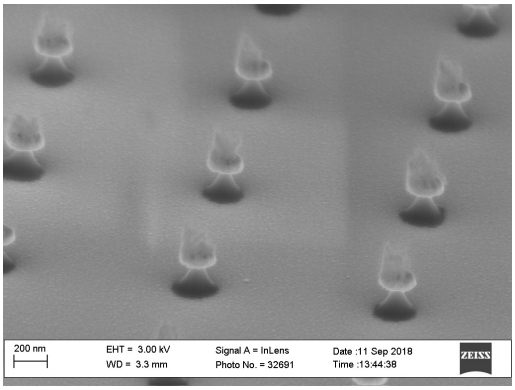

(c) CHF_3 flow of 60 sccm, mask size 200 nm.

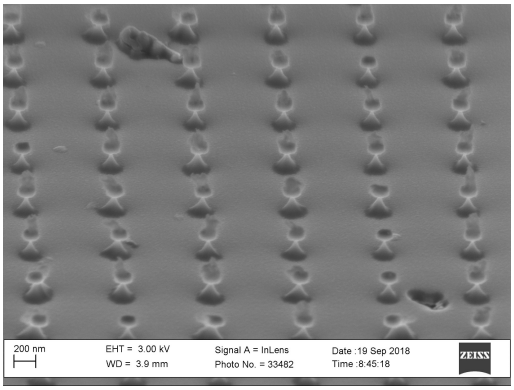

(d) CHF_3 flow of 70 sccm, mask size 150 nm.

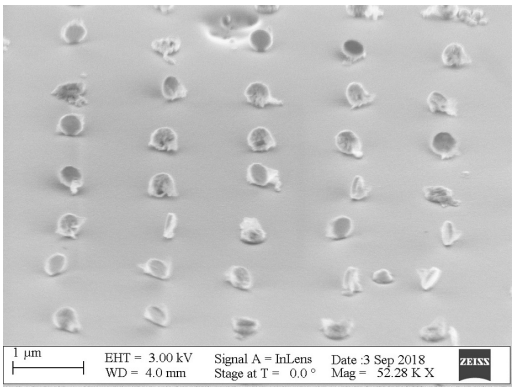

(e) CHF_3 flow of 30 sccm, mask size 200 nm.

Figure 4.4: SEM images of the samples etched with CHF_3 of (a) 40 sccm, (b) 50 sccm, (c) 60 sccm and (d) 70 sccm all at RF power of 30 W. The resulting nanoparticles are cone-shaped. (e) shows a failed etch with 30 sccm CHF_3 at an RF power of 10 W.

arrays were investigated in the SEM in order to find out whether the increase of the etching area led to the microloading effect and therefore to a different anisotropy. It seems to make no difference for the anisotropy.

After investigating these arrays in the SEM, the Cr masks were removed. For this, the samples were left in Cr etchant for 5 minutes and rinsed in a water bath for another minute. After this, they were cleaned with acetone and IPA in order to remove any excess water or Cr etchant. The arrays without the Cr masks were inspected with the SEM. SEM pictures of the samples with and without the Cr masks are shown in Figure 4.5a and Figure 4.5b, respectively. It becomes visible that after the Cr etch the a-Si particles are removed from the substrate, possibly due to a low adhesion between the ITO-substrate and the a-Si.

The final aspect which has to be considered is that the final arrays are fabricated on glass substrates. Since the ITO-layer is conducting, this might make a difference in the etching process. Because of this, the fabrication process was repeated on glass substrates. First, the samples were etched for 5 minutes, but since there were still residues of the a-Si visible by eye, the etching time was increased in steps of 2 minutes, followed by 30 seconds and another 30 seconds until there were no visible residues of a-Si left. After this, the samples were inspected in the SEM. Since the SEM requires a conductive layer, 10 nm aluminum were evaporated onto the samples. In total, two samples on glass substrates were investigated, one before and one after the Cr etch. An SEM image of the sample after the Cr etch can be found in Figure 4.5c. Compared to the case where the arrays have been fabricated onto the ITO substrate, the a-Si arrays stick to the glass substrate. All values for the parameters varied can be found in Table 4.2.

For the transmission measurements one sample has been fabricated on a 75 mm x 20 mm glass substrate with the following RIE parameters: SF_6 flow of 80 sccm, CHF_3 flow of 70 sccm, RF power of 30 W, chamber pressure of 30 mTorr and an etching time of 8 minutes. These parameters correspond to the values given for sample #16 in Table 4.2. The mask diameters were 150 nm and 200 nm and the periodicities were varied from 500 nm to 610 nm in 10 nm steps (see Table 4.1).

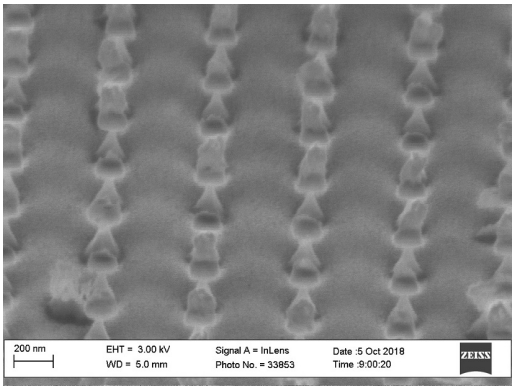

(a) ITO coated substrate of the size 75 mm x 20 mm.

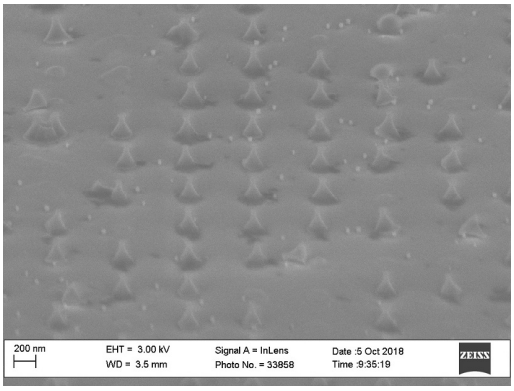

(b) ITO coated substrate of the size 75 mm x 20 mm after Cr etch.

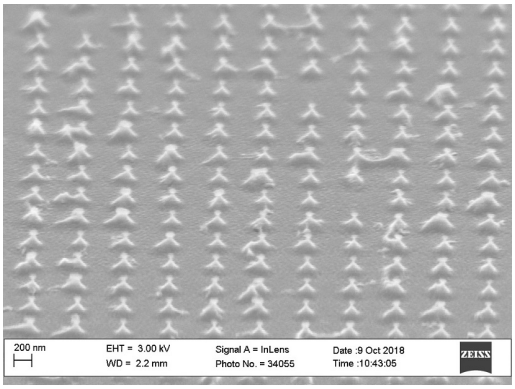

(c) Glass substrate of the size 75 mm x 20 mm after Cr etch.

Figure 4.5: SEM images of (a) ITO coated substrate of the size 75 mm x 20 mm (b) ITO coated substrate of the size 75 mm x 20 mm after etching of the Cr masks and (c) glass substrate of the size 75 mm x 20 mm after etching of the Cr masks. In (b) it becomes visible that the adhesion between the a-Si particles and the ITO coated substrate is not as strong as between the a-Si particles and the glass substrate. All particles have a mask diameter of 150 nm.

#	SF_6 [sccm]	CHF_3 [sccm]	P [W]	p [mTorr]	time [min]	sub-strate	area [mm^2]
1	80	30	10	30	5	ITO	20 x 20
2	80	30	30	30	5	ITO	20 x 20
3	80	40	30	30	5	ITO	20 x 20
4	80	50	30	30	5	ITO	20 x 20
5	80	60	30	30	5	ITO	20 x 20
6	80	70	30	30	5	ITO	20 x 20
7	80	80	30	30	5	ITO	20 x 20
8	80	70	30	25	5	ITO	20 x 20
9	80	70	30	20	5	ITO	20 x 20
10	80	70	30	15	5	ITO	20 x 20
11	80	70	35	30	5	ITO	20 x 20
12	80	70	40	30	5	ITO	20 x 20
13	80	70	45	30	5	ITO	20 x 20
14	80	70	30	30	5+1+ 0.5	ITO	75 x 20
15	80	70	30	30	5+2+ 0.5+0.5	glass	75 x 20
16	80	70	30	30	5+2+ 0.5+0.5	glass	75 x 20

Table 4.2: Values for the varied parameters for the RIE process. The flow rate for SF_6 was held constant while the other parameters were varied. The varied parameters were the flow rate for CHF_3, the RF power P and the chamber pressure p. Increasing the substrate area led to an increasing etching time. The sample which was used in the transmission measurements was fabricated using the parameters specified in #16.

4.3 Dye preparation

Since one goal of this work was to achieve strong coupling between the SLR modes and fluorescent dye molecules, a solution of IR-792 molecules was spin-coated onto the arrays and the light transmission through these was measured. In the following, the preparation of the dye solution is described.

The dye molecules were solved in a PMMA A3 to obtain the desired concentrations of 50, 100 and 200 mM in the solid PMMA film. The concentration is given by the mass of the molecules, solved in the concentration. Therefore, the mass of the dye, dependent on the volume of the mix and the concentration, has to be calculated. The concentration is

$$c_{\mathrm{dye}} = \frac{n_{\mathrm{dye}}}{V_{\mathrm{PMMA}}} = \frac{m_{\mathrm{dye}}}{M_{\mathrm{dye}} V_{\mathrm{PMMA}}} = \frac{m_{\mathrm{dye}} \rho_{\mathrm{PMMA}}}{M_{\mathrm{dye}} m_{\mathrm{PMMA}}}, \tag{4.1}$$

where n_{dye} is the amount of the dye in moles, V_{PMMA} the volume of the PMMA in which the dye is dissolved into, and m_{dye} and M_{dye} are the mass and the molar mass of the dye, respectively. ρ_{PMMA} is the density of PMMA and m_{PMMA} the mass of PMMA. Since the PMMA is mixed in anisole with a portion of 3% PMMA, the mass of PMMA is

$$m_{\mathrm{PMMA}} = 0.03 m_{\mathrm{mix}} = 0.03 \rho_{\mathrm{mix}} V_{\mathrm{mix}} = 0.03 \left(1 + \frac{0.03}{0.97}\right) \rho_{\mathrm{a}} V_{\mathrm{mix}}, \tag{4.2}$$

where ρ_{mix} is the density of the mixture, V_{mix} the volume of the mixture and ρ_{a} the density of anisole. This leads to the following expression for the mass of the dye

$$m_{\mathrm{dye}} = \frac{c_{\mathrm{dye}} m_{\mathrm{PMMA}} M_{\mathrm{dye}}}{\rho_{\mathrm{PMMA}}} = 0.03 \left(1 + \frac{0.03}{0.97}\right) \frac{\rho_{\mathrm{a}}}{\rho_{\mathrm{PMMA}}} V_{\mathrm{mix}} M_{\mathrm{dye}} c_{\mathrm{dye}}. \tag{4.3}$$

The values used for the calculation according to Eq. 4.3 can be found in Table 4.3. After measuring the dispersion relations of the samples without any dye and estimating the energy of the SLRs, IR-792 has been chosen as a dye because of its appropriate absorption maximum location at $\lambda = 804$ nm or $E = 1.54$ eV. The absorbance spectrum of the dye is shown in Figure 4.6.

After mixing the dye in PMMA A3, 75 μL of the mix was spin coated on top of the sample at 3000 RPM for one minute. The samples were left for evaporating excess liquid for 30 minutes before further usage. To change the dye, the samples were cleaned with acetone and a dye mix of another concentration was spin coated on top. In order to minimize impurities by old dye molecules, the dye mix with the lowest concentration of 50 mM was used first and the dye mix with the highest concentration of 200 mM was used last.

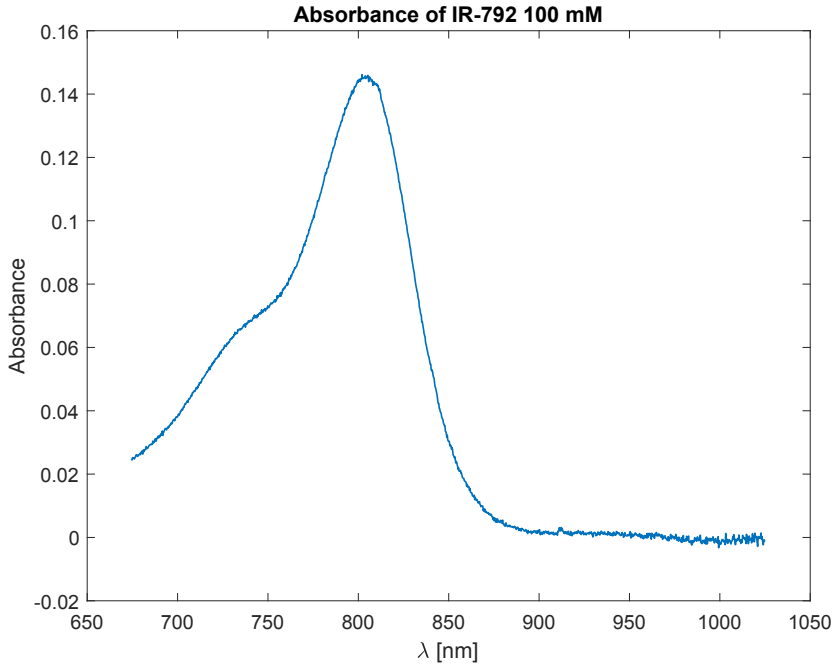

Figure 4.6: Measured absorbance spectrum of IR-792 of a concentration of 100 mM. The absorbance peak is at $\lambda = 804$ nm or at $E_{abs} = 1.54$ eV.

ρ_{PMMA}	1.18 g/ml [36]
ρ_{a}	0.995 g/ml [37]
M_{dye}	717.37 g/Mol [38]

Table 4.3: Values used for the calculation of the mass of the dye for solving it in PMMA A3.

Chapter 5

Measurements

In this chapter, the transmission measurement setup and the procedure of taking the measurements are explained. In addition, some important notes on how the data was processed will be given.

5.1 Transmission measurement setup

After fabricating the samples, their light transmission is measured to obtain the dispersion relations. To understand the measurements, the measurement setup is described, followed by a description of how the measurements were done and analysed. The measurement setup is depicted in Figure 5.1. The sample is mounted on a sample holder which is adjustable in x, y and z-directions with micrometer screws in order to bring it into focus. The sample is illuminated by a light source, which is a halogen lamp with a spectral range over the visible and near infrared spectrum. The sample is immersed in index matching oil between two glass substrates in order to provide a symmetrical index environment with a refractive index of $n = 1.51$. The index matching oil is necessary, since the asymmetry between the refractive indices of the substrate and superstrate surrounding the nanoparticle arrays leads to a reduction or even suppression of the diffraction in the arrays [24]. The light transmitted through the sample is led through and focused by the objective and a lens L1. The focal point of the objective is on the sample. The lens L1 is placed such that its distance equals the sum of the focal lengths of the objective and lens. A real image is formed at the backside of L1. The iris which is manually adjustable is used to restrict the incoming light to only that area which shall be examined with the charge-coupled device (CCD) camera and the spectrometer. The polarizer is optionally used to investigate the transmitted light on TE and TM modes. The beam splitter splits the

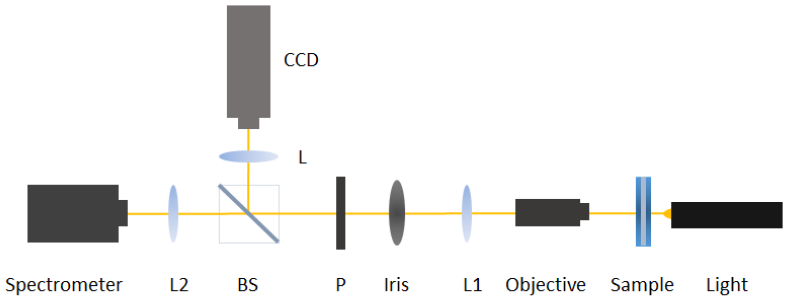

Figure 5.1: Schematic of the setup for the transmission measurement.

light into two paths: one, which goes to the CCD camera, where the area which is illuminated by the halogen lamp and led through the optical system can be observed and focused in real space. The other part of the ray is led through another lens L2. The lens L2 is placed at the distance from L1 such that it equals the sum of their focal lengths. L2 leads the light into the spectrometer which is placed at the back focal plane of L2. This setup ensures that all light rays that leave the sample at the same angle meet at the same point of the spectrometer slit. Therefore, the position on the slit determines the angle under which the light comes from the sample.

In the spectrometer the light coming from the sample under the angle θ is separated by wavelengths and guided by a mirror system to the CCD port of the spectrometer, where it is detected. Now the relation between the incident angle θ and the pixel lines of the spectrometer CCD has to be determined. Usually, the k-space measurements are symmetrical around $k_{||} = 0$, so the pixel line p_0 which describes the centre of the back focal line is known. A second reference point p_{max} can be determined if the edge of the k-space image is visible with the corresponding angle θ_{max} which is given by

$$\theta_{max} = \arcsin\left(\frac{NA}{n}\right), \tag{5.1}$$

where NA is the numerical aperture of the objective and n the refractive index. For any pixel line p with the corresponding angle θ one gets

$$\theta = \arctan\left(\frac{p - p_0}{p_{max} - p_0} \tan\theta_{max}\right). \tag{5.2}$$

Thus, it is possible to measure the wavelength or energy in dependence on the k_y vectors of the light with the spectrometer. Both the CCD camera and the spectrometer are connected to a computer over which they are operated and the data is collected.

5.2 Experimental procedure

The measurements were conducted as following: First, the sample was mounted on the sample holder and illuminated by the light source. With the CCD (as depicted in Figure 5.1) it was possible to see the image coming from the objective. Using this CCD image one could bring the sample into a position such that one nanoparticle array was visible and brought into focus. After focusing on the array, the iris was closed so far that only the area which is covered by the array was visible. The slit of the spectrometer was opened to 50 μm and the signal coming from the array was measured. Then, the sample holder was moved in x and y-direction to measure another array. The width of the iris was kept unchanged. It was only opened to focus on a new sample after it was mounted on the sample holder. Additionally, a reference measurement was conducted for each sample. For that, the sample was moved so, that an area of the sample without arrays was visible and measured. If the samples were spin-coated with the dye molecules, two references were taken: one through the area with dye and one without dye. While spincoating the dye solution onto the samples, there typically were areas on the glass substrates without dye. Therefore, it was possible to take both reference measurements for each sample. Finally, background was measured by blocking the direct light path. This ensures that all surrounding light sources such as computer screens and the indirect light coming from the light source are measured and can be subtracted from the result.

5.3 Data processing

The analysis of the obtained .spe files was done with MATLAB using a code which was developed in our group. The transmission measurements through the arrays had to be corrected by the background measurements and divided by the reference measurements

$$T_{sample} = \frac{I_{array} - I_{background}}{I_{reference} - I_{background}}, \tag{5.3}$$

where I_{array}, $I_{reference}$ and $I_{background}$ are the intensities measured by the spectrometer of the array, glass and the background, respectively. Since the total transmittance of a system consisting of non-interacting materials is the product of the single transmittances of the materials, this is legitimate. The extinction cross-section for one unit cell is defined as [12]

$$\sigma_{ext} = (1 - T_{sample})p^2, \tag{5.4}$$

where p is the periodicity of the array. In case of the samples with the dye molecules spincoated on top, the extinction cross-section of the dye has to be subtracted of the extinction cross-section of the array in order to substract the uncoupled contribution:

$$\begin{aligned}\sigma_{ext,system} &= \sigma_{ext,sample} - \sigma_{ext,dye} \\ &= (1 - T_{sample}) - (1 - T_{dye}) = T_{dye} - T_{sample} \\ &= \frac{I_{dye} - I_{background}}{I_{reference} - I_{background}} - \frac{I_{sample} - I_{background}}{I_{reference} - I_{background}},\end{aligned} \tag{5.5}$$

where I_{dye} is the intensity measured by the spectrometer through the substrate covered with dye but without any nanoparticle arrays [12]. This ensures that the resonances of the strongly-coupled systems are visible through the absorption spectrum of the dye. Peaks in the extinction spectrum resemble the points where the scattering and absorption of the light is at its maximum and show therefore the resonant modes of the system.

5.4 Fitting process for determining the Rabi splitting

After adding dye molecules onto the nanoarrays, the coupled system forms the Rabi splitting in the dispersion relation (see Section 2.2). In order to determine whether or not the system is in the strong coupling regime, the splitting has to increase linearly with the square root of the concentration of the dye molecules, see Equation 2.21. The Rabi splitting can be obtained from the experimental data as described in the following.

First, the upper branches of the SLRs of the dispersions of the arrays without dye molecules are obtained. The upper branches of the SLRs refer to the dispersion branches of the TE modes with higher energies than at the Γ-point, see for instance Figure 3.3. It is sufficient to only fit the upper branches, since the absorption energy of the emitters is so high that only the upper branches of the SLRs are involved in the coupling. For this, the peaks in the dispersions are obtained by using a peak finding function in Matlab. Since the peak finding function finds all peaks, i.e. also the lower branches of the TE modes as well as the TM modes, the peaks need to be sorted manually. After sorting, the peaks are fitted according to a three-coupled-modes model. It consists of a 3 x 3 matrix where the original LSPR and the two SLR energies are on the diagonal elements and the coupling coefficients are on the off-diagonal elements. The resonances of the coupled system are given by the eigenvalues of this matrix. With the least-square-sum method

the difference between the eigenvalues of the matrix and the peaks found with the peak finding function is minimized [12]. The minimization is done with fminsearch, a minimum finding function in Matlab which also gives the residuals of the fit.

After the SLRs of the arrays without dye molecules are obtained, the Rabi splitting has to be obtained from the dispersions of the arrays with dye molecules. For this, again, the peaks in the dispersions are obtained and sorted manually such, that only the upper branches of the TE modes are involved in the fitting. A two-coupled-modes model is applied where the diagonal elements of the 2 x 2 matrix are the energies of the upper branches of the SLRs, E_{SLR+}, which are obtained from the dispersions of the arrays without dye molecules, and the absorption line of the dye molecules, E_{dye}. The off-diagonal elements give the coupling coefficient c:

$$M = \begin{bmatrix} E_{SLR+} & c/2 \\ c/2 & E_{dye} \end{bmatrix}$$

As before, the eigenvalues of the matrix give the resonances of the coupled system. The difference between the eigenvalues and the peaks found with the peak finding function is minimized using the least-square-sum method and the fminsearch function in Matlab. The splitting is the same as the coupling coefficient which corresponds to the coupling strength.

Chapter 6

Results of transmission measurements

This chapter presents the results of the transmission measurements of the samples fabricated as described in Chapter 4. First, the dispersions of the Au, Ge and a-Si nanoarrays, as defined in Table 4.1, are measured without dye molecules on top. These dispersions are compared to each other with respect to their response quality, i.e. linewidth and Q-factor. Secondly, the dispersion relations of Au, Ge and a-Si nanoarrays with dye molecules on top will be presented.

6.1 Dispersions of arrays without molecules

6.1.1 Dispersions of gold nanoarrays

In the following the dispersions of the bare arrays, i.e. without dye molecules on top, are presented for Au, Ge and a-Si and the results are discussed briefly. It is important to note that the Au arrays have a two nm thick layer of Ti between the substrate and the Au nanoparticles in order to improve the adhesion. The Ge samples do not have that extra layer of Ti, unless they are referred to as Ge(Ti) (see Table 4.1). Figure 6.1 shows measured dispersions of the fabricated Au nanoparticle arrays of different periodicities and diameters. Figure 6.1 shows arrays made of particles with a diameter of 100 nm and periodicities of 550, 560, 570 and 580 nm. The expected red-shift of the dispersion is clearly visible as well as the TM and TE modes. Figure 6.2 shows the dispersion of an arrays consisting of particles with a diameter of 140 and 180 nm and a periodicity of 570 nm. Compared to the dispersions of the arrays with smaller diameters, the linewidth is larger

with larger diameters and the TM mode is not as distinctive as before. In addition, the modes undergo a red-shift with increasing diameter.

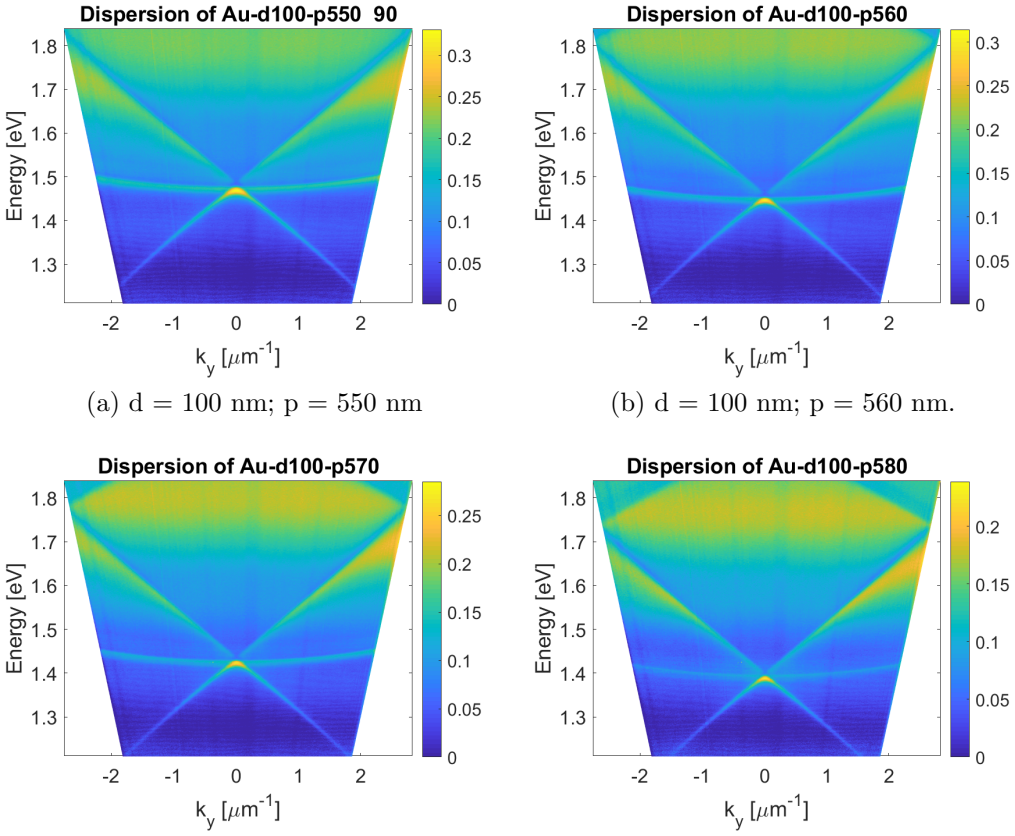

(a) d = 100 nm; p = 550 nm

(b) d = 100 nm; p = 560 nm.

(c) d = 100 nm; p = 570 nm

(d) d = 100 nm; p = 580 nm

Figure 6.1: Measured dispersions of gold nanoparticle arrays of different periodicities. The used sample was sample #1 (see Table 4.1).

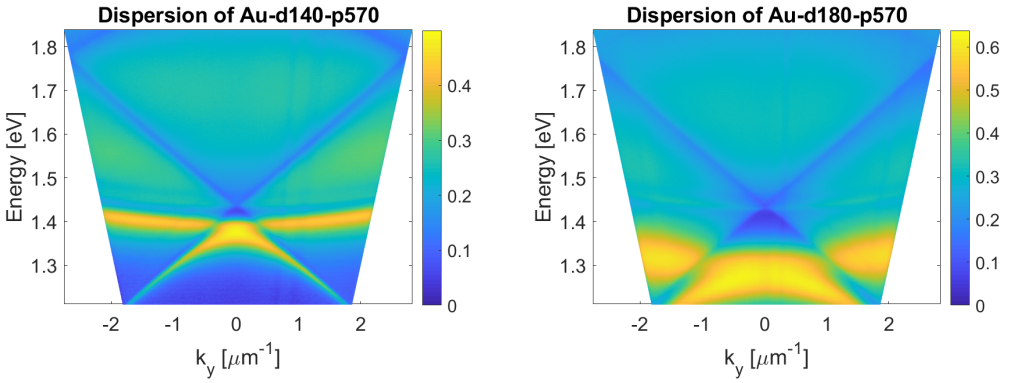

(a) d = 140 nm; p = 570 nm (b) d = 180 nm; p = 570 nm

Figure 6.2: Measured dispersions of gold nanoparticle arrays of different diameters. The used sample was sample #1 (see Table 4.1).

6.1.2 Dispersions of germanium nanoarrays

The dispersion relations of the Ge arrays show the same features as the Au arrays. Measured dispersions of arrays made of particles with a diameter of 150 nm and periodicities of 560, 570, 580 and 590 nm are shown in Figure 6.3. These dispersions show only the TE modes since a polarizer was used during these measurements. Similar to the Au nanoarrays, the expected red-shift with increasing periodicity is visible here as well. Figure 6.4 shows the dispersion of an array consisting of particles with diameters of 150 and 200 nm and a periodicity of 570 nm. The linewidth broadens with increasing particle diameter. Compared to the Au arrays, the Ge arrays show similar sharp features. In addition, there is a broad peak around 1.8 eV visible for Au, which corresponds to the LSPR of Au (see Section 3.2), while there is no peak like this visible for the Ge arrays.

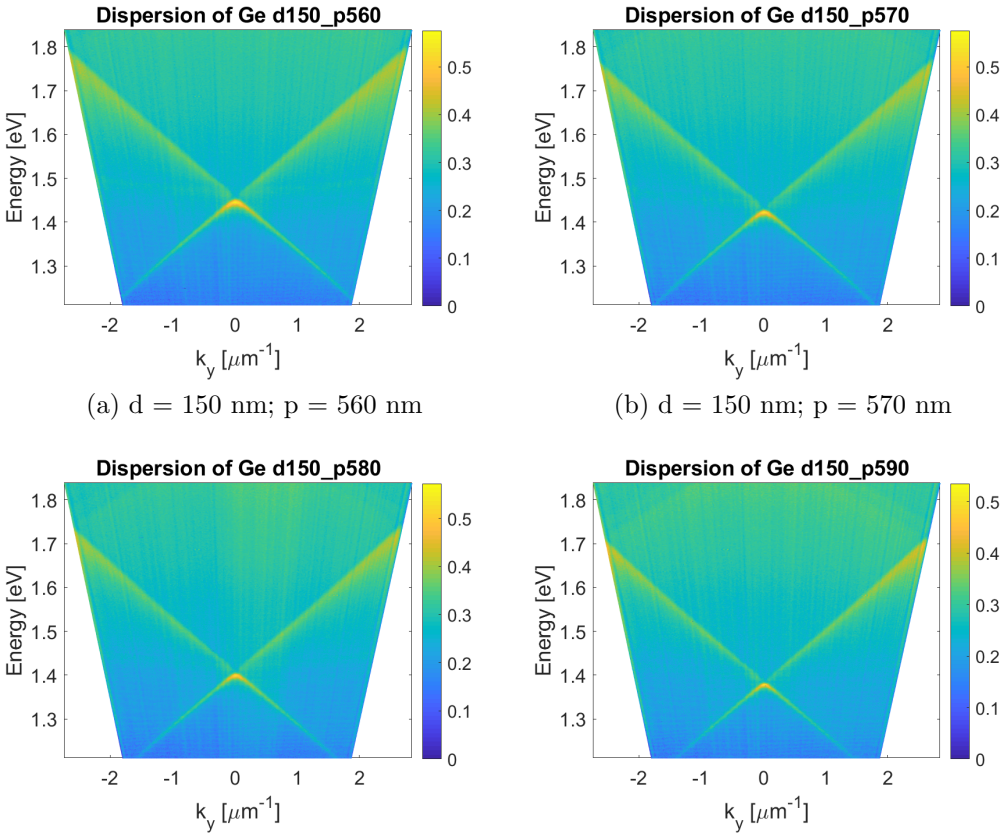

(a) d = 150 nm; p = 560 nm

(b) d = 150 nm; p = 570 nm

(c) d = 150 nm; p = 580 nm

(d) d = 150 nm; p = 590 nm

Figure 6.3: Measured dispersions of germanium nanoparticle arrays of different periodicities. Sample #2 was used (see Table 4.1).

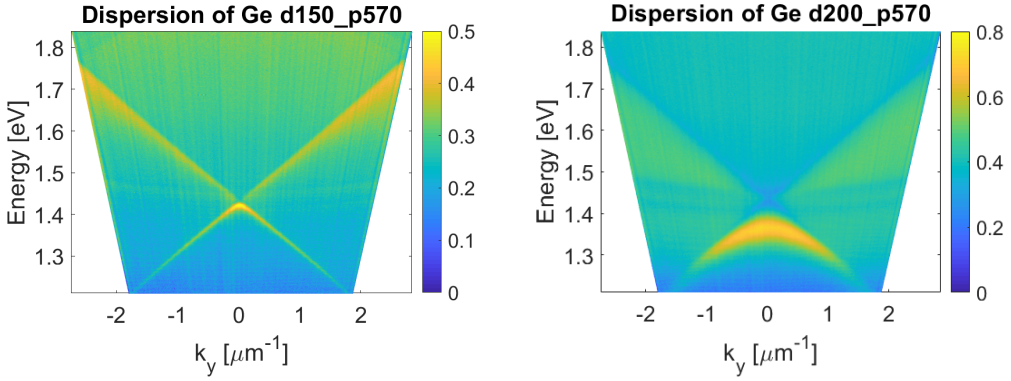

(a) d = 150 nm; p = 570 nm (b) d = 200 nm; p = 570 nm

Figure 6.4: Measured dispersions of germanium nanoparticle arrays of different diameters. The used sample was sample #2 (see Table 4.1).

In addition, Figure 6.5a shows measured dispersion of Ge(Ti) nanoarrays, i.e. the Ge nanoarrays with a 2nm thick layer of Ti between Ge and the substrate (see Section 4.1), with a diameter of 150 nm and periodicity 570. Figure 6.5b shows the dispersion of an array of only Ge with the same diameter and periodicity. The the spectral features of Ge(Ti) are less sharp, i.e. the linewidth is broader compared to the spectral features of Ge.

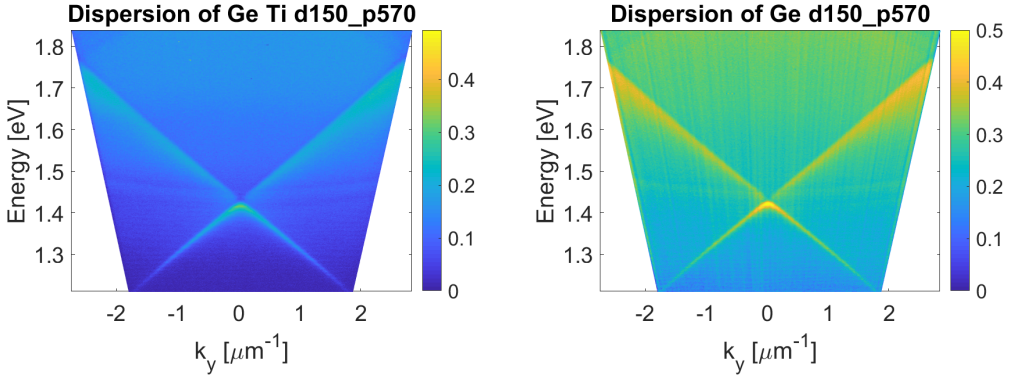

(a) Ge with Ti layer. (b) Ge without Ti layer.

Figure 6.5: Measured dispersions of Ge(Ti) and Ge nanoparticle arrays with a particle diameter of 150 nm and a periodicity of 570 nm. The used samples were #3 and #2, respectively (see Table 4.1).

6.1.3 Dispersions of a-Si nanoarrays

The dispersion relations of the a-Si arrays are shown in Figure 6.6 for arrays with periodicities of 550, 560, 570 and 590 nm. The mask diameter was 150 nm. Similar to the Au, Ge and Ge (Ti) nanoparticle arrays, the dispersions undergo a red-shift with increasing periodicity. It is obvious that that the dispersion in Figure 6.6d is much sharper than the others. This is most probably due to a more successful etching of exactly this array compared to the other ones. Figure 6.7 shows the dispersions of arrays with a periodicity of 570 nm and mask diameters of 150 and 200 nm. As before, the increasing mask size leads to a broadened linewidth. However, the broadening is not as extreme as in the Ge or Au arrays. A reason for this might be that the a-Si particles are cone-shaped and the increase of the mask diameter leads to a truncated cone (see Chapter 4). Therefore, the the tip of the particles is still much more confined and the SLRs are much sharper than of the cylindrical shaped SLRs of the Au and Ge nanoarrays. Another reason could also be, that a-Si has lower losses than Au and Ge.

In the following, a more detailed comparison between the nanoparticle arrays of Au, Ge and a-Si is presented.

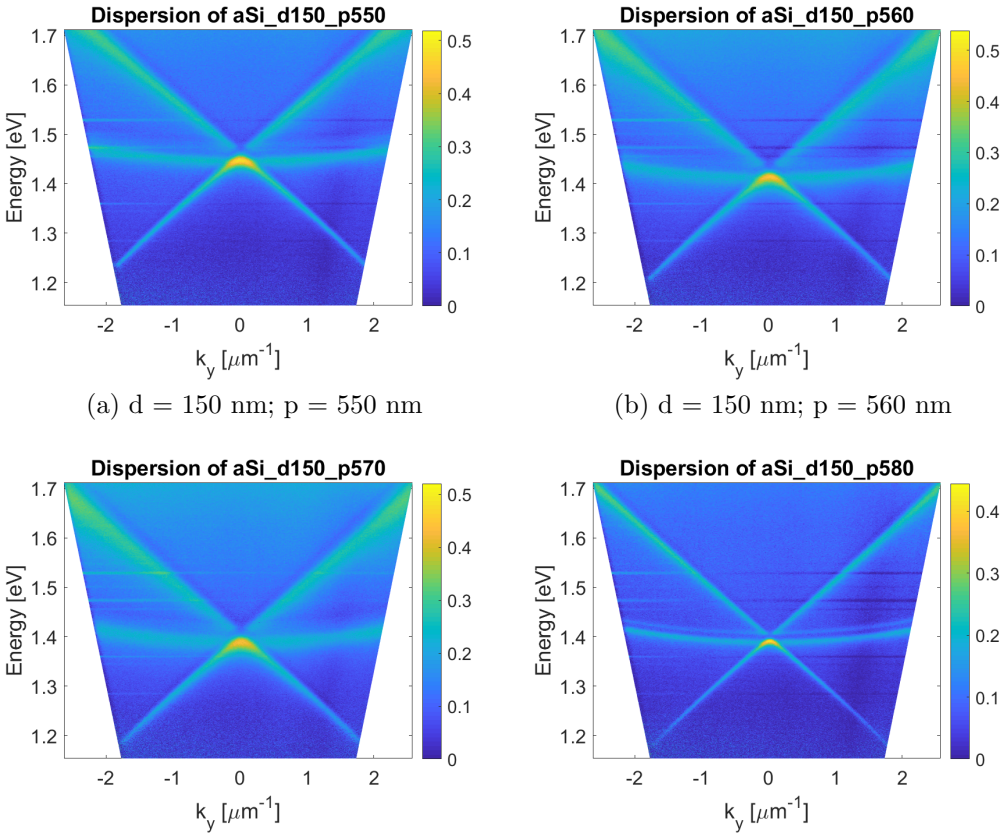

(a) d = 150 nm; p = 550 nm

(b) d = 150 nm; p = 560 nm

(c) d = 150 nm; p = 570 nm

(d) d = 150 nm; p = 580 nm

Figure 6.6: Measured dispersions of a-Si nanoparticle arrays of different periodicities. The used sample was #4 (see Table 4.1).

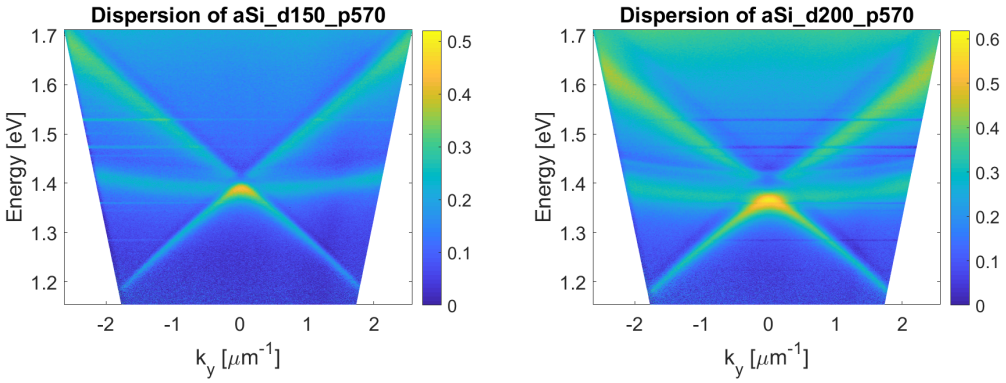

(a) d = 150 nm; p = 570 nm (b) d = 200 nm; p = 570 nm

Figure 6.7: Measured dispersions of a-Si nanoparticle arrays of different mask diameters. The used sample was sample #4 (see Table 4.1).

6.1.4 Comparison of the dispersions of Au, Ge and a-Si

6.1.4.1 Spectra at k_y=0

Figure 6.8 shows the spectra of Au, Ge, Ge (Ti) and a-Si samples at the Γ-point. Here, the sharp peaks correspond to the SLRs which result from the constructive interferences of the scattered light from each nanoparticle in the array (see Section 3.2). The broad peak in Figure 6.8a corresponds to the LSPR of one cylindric gold particle with a diameter of 100 nm and a height of 50 nm (see Section 3.2). Since the LSPR is not visible in Figures 6.8b, 6.8c and 6.8d, one can assume that the single particle resonance lies at much higher energies than the SLRs of the arrays and is much broader than the LSPR of gold.

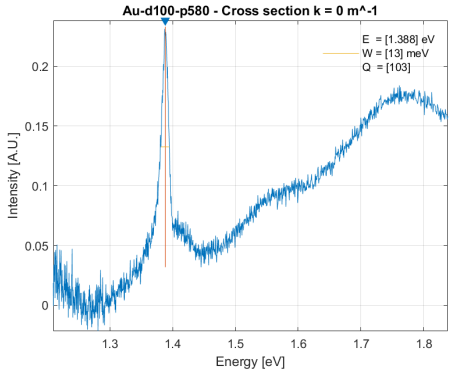

(a) Γ-point spectrum for Au, d = 100 nm; p = 580 nm.

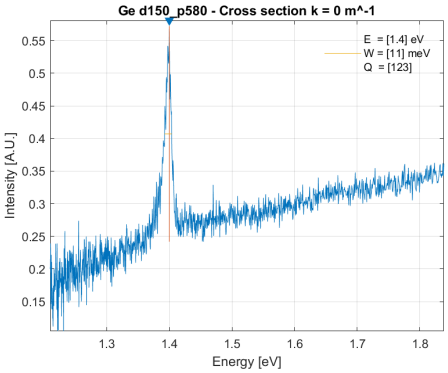

(b) Γ-point spectrum for Ge, d = 150 nm; p = 580 nm.

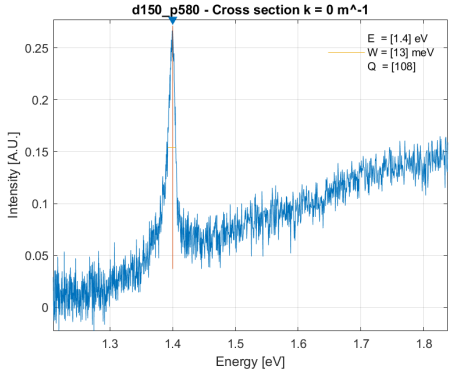

(c) Γ-point spectrum for Ge (Ti), d = 150 nm; p = 580 nm.

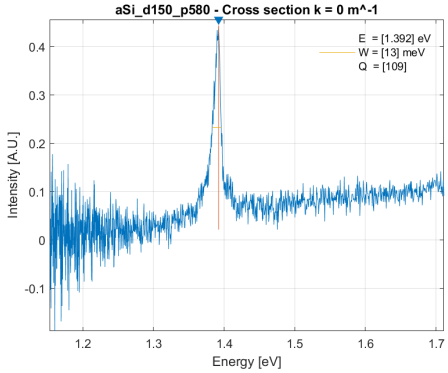

(d) Γ-point spectrum for a-Si, mask size d = 150 nm; p = 580 nm.

Figure 6.8: Γ-point spectra for (a) Au, (b) Ge, (c) Ge (Ti) and (d) a-Si.

6.1.4.2 Energy, FWHM, Q-factor at k_y=0

A way to check whether the SLRs follow the expected behaviour is to plot the energy versus periodicity. It is important to note that up to this point the diameters, periodicities and mask sizes were the nominal values, i.e. the ones used in the layouts for the EBL. In order to compare the experimental data to the theory, the true values for the diameters and periodicites need to be known. For this, one of the samples was measured with the SEM. A result was that the periodicites are approximately 10 nm larger and the diameters approximately 5 nm. In the following, the periodicities are presented with the true values while the diameters are the nominal values in order to keep things simpler. Figure 6.9a shows energy versus periodicity for Au arrays with a diameter of 100 nm, for Ge and Ge (Ti) arrays with a diameter of 150 nm and for a-Si arrays with a mask diameter of 150 nm. The Au, Ge and Ge (Ti) arrays follow the same behaviour as expected theoretically, which means that $E \propto \frac{\hbar c}{np}$ (see Equation (3.6)). The energies of the a-Si nanoparticle arrays are located below the theoretical values. This might be due to the fact that the arrays consist of cone-shaped particles and not cylinders as the other ones. Another reason could be that the RIE process is rather unreliable and a-Si residues between the particles distort the SLRs.

A way to compare the quality of the SLR modes is the full width at half maximum (FWHM) of the peaks and the quality factor or Q-factor which is defined by $Q = \frac{\text{FWHM}}{E}$. The FWHM versus periodicity and Q-factor versus periodicity are shown in Figures 6.9b and 6.9c, respectively. Figure 6.9d shows the energy versus Q-factor. Generally, a higher Q-factor or a smaller FWHM means that the energy losses in the system are lower [39]. As can be seen from the figures, the highest Q-factor is achieved by the Ge arrays followed by the Au arrays. The Ge (Ti) and a-Si arrays have a much lower Q-factor. The lowest FWHM for Ge are at 7 meV, for Au at 10 meV and for Ge (Ti) and a-Si at 13 meV. The highest Q-factor for Ge is 165, for Au 130, for Ge (Ti) 108 and for a-Si 109. In addition, it is obvious that the general trend of a-Si is bad, most probably due to the fabrication.

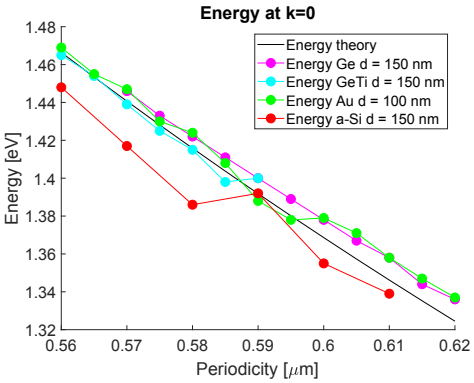

(a) Energy vs. periodicity.

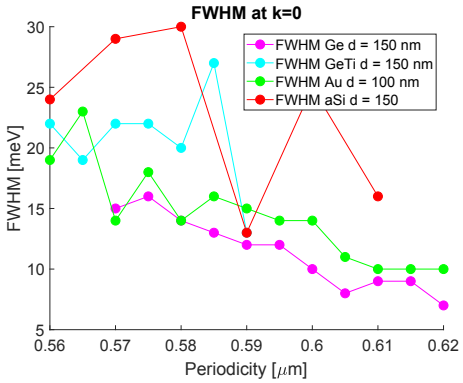

(b) FWHM vs. periodicity.

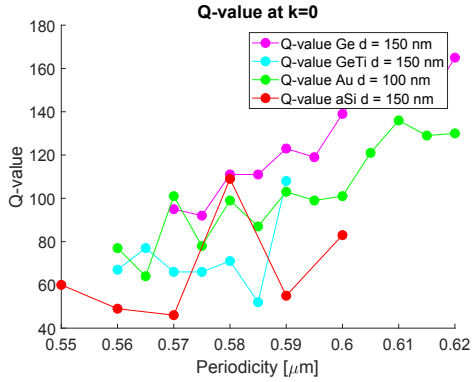

(c) Q-factor vs. periodicity.

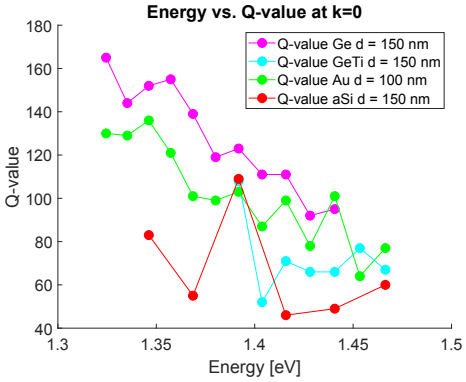

(d) Q-factor vs. energy.

Figure 6.9: (a), (b) and (c) show the energy, the full width at half maximum (FWHM) and Q-factor, respectively, of the different materials as a function of the periodicity for $k_y = 0$. (d) shows the Q-factor as a function of the energy for $k_y = 0$. The diameter of the Au particles is 100 nm, the diameter of the Ge and Ge (Ti) particles is 150 nm and the mask size for the a-Si particles is 150 nm.

Energy, FWHM, Q-factor at k_y=0.5

Figure 6.10 shows the same plots of the same arrays for $k_y = 0.5$ considering the lower branch of the TE mode. The general behaviour of energy, FWHM and Q-factor as a function of the periodicity is the same as for $k_y = 0$. Likewise, a-Si appears to have the lowest Q-factors and largest FWHM at $k_y = 0.5$. Ge (Ti) has slightly higher Q-factors and lower FWHM for $k_y = 0.5$ than for $k_{y=0}$. The Q-factors and FWHM for Ge and Au are very similar to each other for $k_y = 0.5$. The lowest FWHM for Ge are at 6 meV, for Au at 7 meV, for Ge (Ti) at 9 meV and for for a-Si at 9 meV. The highest Q-factor for Ge is 207, for Au 183, for Ge (Ti) 147 and for a-Si 142.

This already shows that the Ge nanoarrays are as good or even slightly better than the Au nanoarrays due to Ge being a low-loss material. The Ge (Ti) arrays are not as good perhaps because the Ti leads to additional single particle resonances and therefore the overall response of the system decreases. The dispersions of the a-Si nanoparticle are probably worse due to the fact that the RIE process is not absolutely reliable. This becomes obvious since some arrays seem to have very nice features while others are comparatively bad (see Figure 6.6). Also the SEM images show that after the RIE process, there are a-Si residues between the particles which leads to a less uniform array and therefore the dispersion features become less prominent.

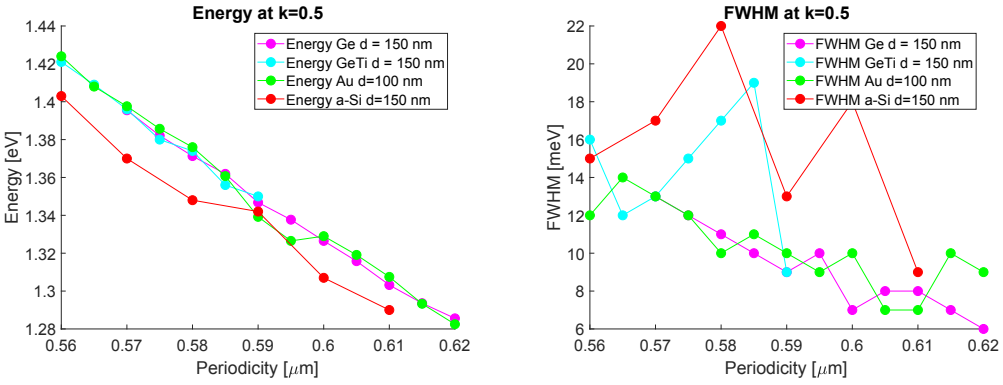

(a) Energy vs. periodicity.

(b) FWHM vs. periodicity.

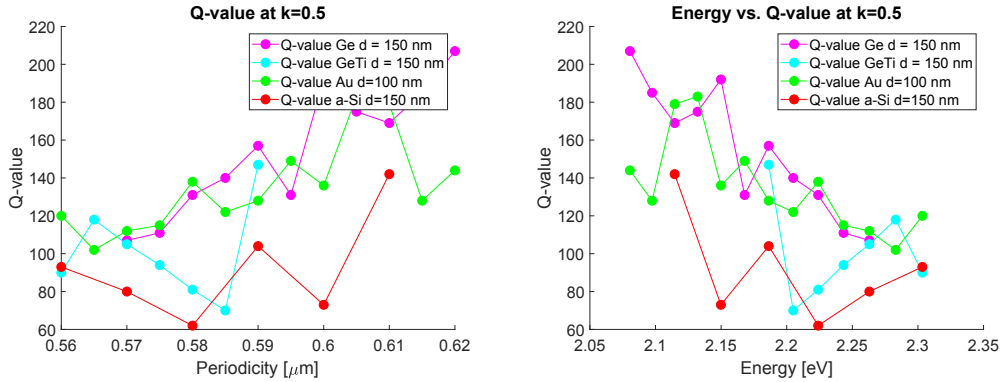

(c) Q-factor vs. periodicity.

(d) Q-factor vs. energy.

Figure 6.10: (a), (b) and (c) show the energy, FWHM and Q-factor, respectively, of the different materials as a function of the periodicity for $k = 0.5$. (d) shows the Q-factor as a function of the energy for $k = 0.5$. The diameter of the Au particles is 100 nm, the diameter of the Ge and Ge(Ti) particles is 150 nm and the mask size for the a-Si particles is 150 nm.

6.2 Dispersions with dye molecules

After having discussed the dispersions of the bare arrays and having ensured that the dispersions are of good quality, i.e. the dispersions are sharp and well visible, the dye molecules were spin-coated onto the samples as described in Section 4.3 and the transmission through the samples was measured. In the following, the dispersions of Au, Ge and a-Si nanoparticle arrays with dye molecules of the concentrations 0 mM, 50 mM, 100 mM and 200 mM are presented.

6.2.1 Dispersions of gold nanoarrays

Figure 6.11 shows the dispersion of an Au nanoparticle array with a nominal particle diameter of 100 nm and a nominal periodicity of 600 nm without dye molecules (Figure 6.11a) and with dye molecules of concentrations of 50 mM, 100 mM, 200 mM in Figures 6.11b, 6.11c and 6.11d, respectively. The results of this array are presented here, since it gave the nicest looking dispersions for all concentrations. In addition, it provides the most narrow responses (see e.g. Figure 6.9b).

It is visible that with increasing concentration the upper branches of the dispersions become less visible at the absorption line of the dye ($E_{abs} = 1.54$ eV). In addition, the lower parts of the upper branches begin to clearly bend at concentrations of 100 mM and 200 mM, as expected (see Chapter 2). The avoided crossing becomes visible and therefore one can assume that this system is in the strong coupling regime. The double line at the TM mode is probably due to a tilt in the sample stage. Another explanation could be that both the bright and the dark mode (see Section 3.2) provide TM modes but usually the dark mode does not couple out to the far-field.

The fitting process (see Section 5.4) is already applied. Figure 6.11a shows the fitting of the upper branches without dye molecules. The diagonal red dashed lines are the theoretical first DOs, the horizontal dashed line the LSPR, the squares depict the peaks involved in the fitting process and the solid black lines the fitted SLRs. Figures 6.11b-6.11d show the fitting of the SLR-emitter system. The black circles depict the peaks involved in the fitting, the horizontal red dashed line the absorption energy of the emitter and the diagonal red dashed line is the upper branch of the SLRs of the first DOs obtained from the fitting of Figure 6.11a. The solid black lines depict the new modes between SLRs and dye molecules. From the plot it becomes obvious that the fitting procedure is worse for the 200 mM case, since the fitted curve does not follow the dispersions. The exact reason for this is

unknown but needs to be investigated further. The values for the splitting can be found in Table 6.1.

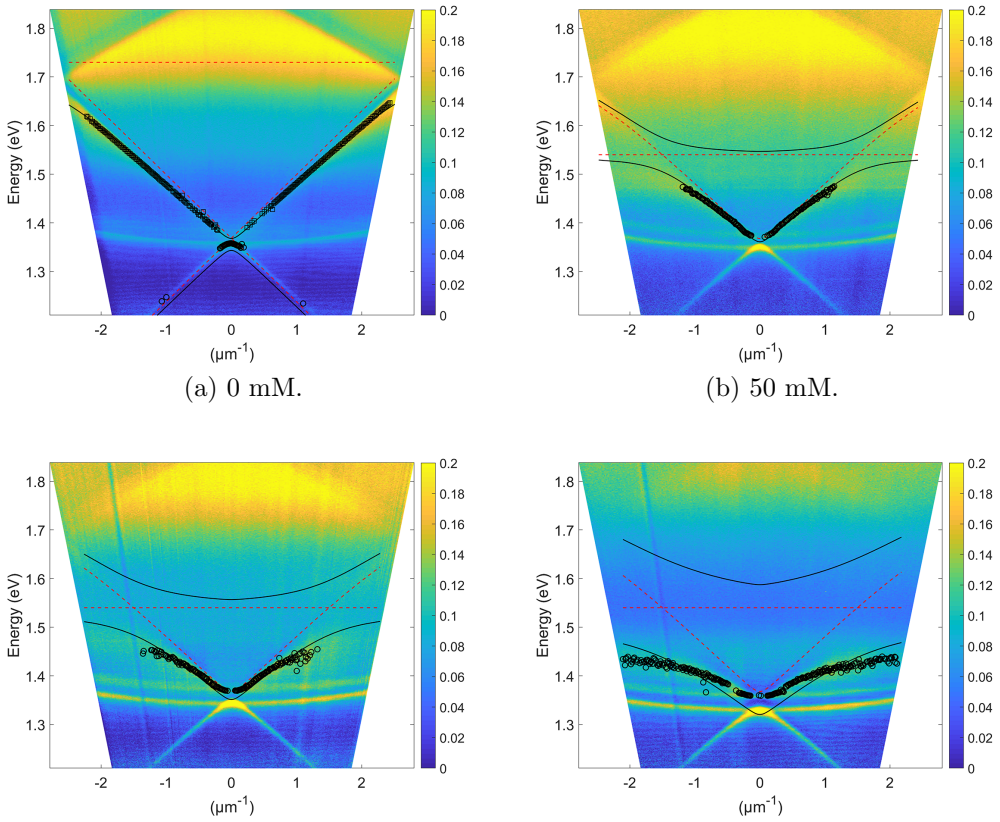

(a) 0 mM. (b) 50 mM.

(c) 100 mM. (d) 200 mM.

Figure 6.11: Dispersions of an Au array with a particle diameter of 100 nm and a periodicity of 600 nm (a) without dye molecules on top, (b) 50 mM (c) 100 mM (d) 200 mM dye molecules on top. The used sample was sample #1 (see Table 4.1).

6.2.2 Dispersions of germanium nanoarrays

The fitted dispersions of a Ge nanoparticle array without the Ti layer are shown in Figure 6.12 for different dye concentrations. The array consists of particles with a nominal diameter of 150 nm and a nominal periodicity of 600 nm. The dispersions show the same features of strong coupling as the dispersions of the Au arrays. This array is presented, since it has the same periodicity as the Au array presented before and provides a similar good linewidth (see e.g. Figure 6.9b).

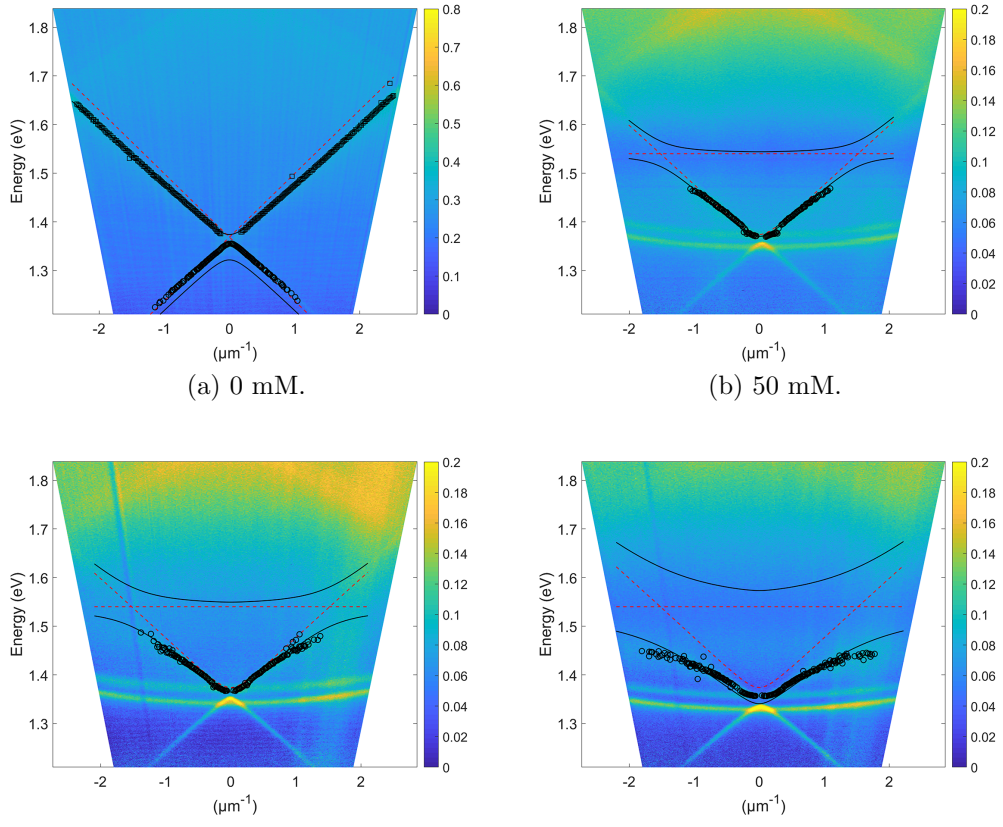

(a) 0 mM. (b) 50 mM.

(c) 100 mM. (d) 200.

Figure 6.12: Dispersions of an Ge (without the Ti layer) array with a particle diameter of 150 nm and a periodicity of 600 nm (a) without dye molecules on top, (b) 50 mM (c) 100 mM (d) 200 mM dye molecules on top. The used sample was sample #2 (see Table 4.1). The horzontal features in (a) and (b) are background radiation which show up probably due to a failed background subtraction.

6.2.3 Dispersion of amorphous silicon nanoarrays

Figure 6.13 shows the dispersions of an a-Si nanoparticle array with dye molecules on top with different concentrations after the fitting process. The array is of the mask diameter 150 nm and with a nominal periodicity of 580 nm. Also these arrays show the an increasing splitting with increasing dye concentration, which is characteristic for strong coupling. This array was chosen, since it showed the most narrow features (see Section 6.1.4, Figure 6.9). A smaller periodicity means that the dispersion features are blueshifted. This means that the strong coupling takes place at another position in the spectrum but the bending and splitting stays the same.

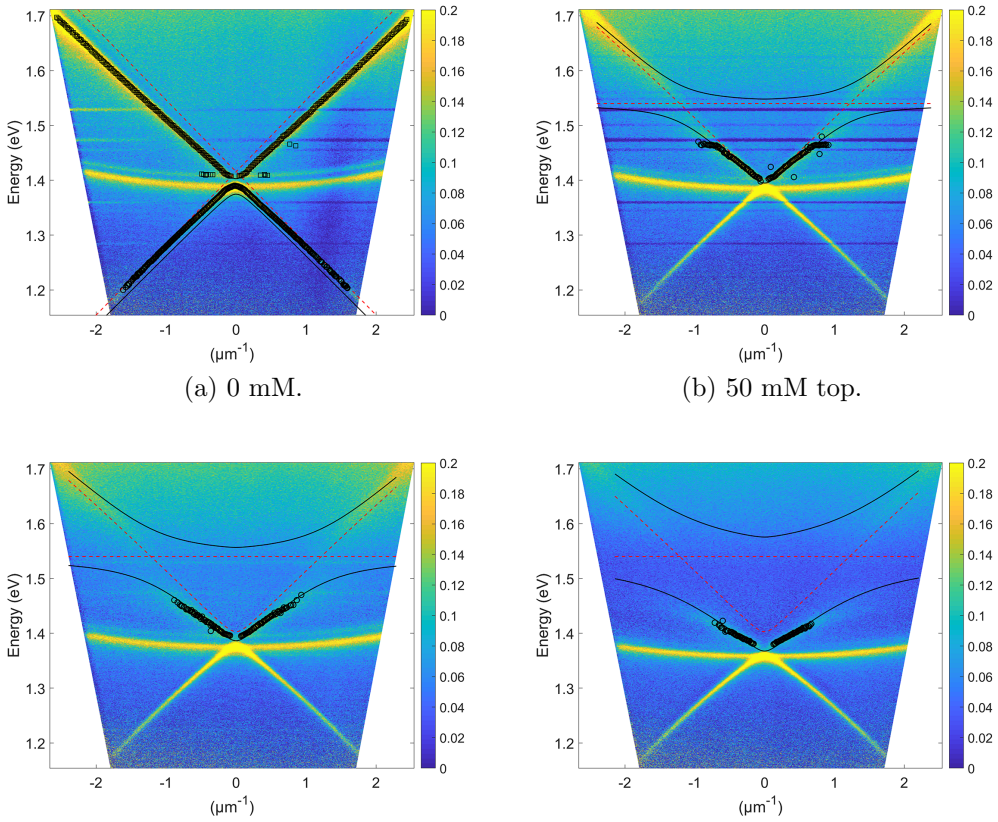

(a) 0 mM. (b) 50 mM top.

(c) 100 mM. (d) 200 mM.

Figure 6.13: Dispersions of an a-Si array with a mask size of 150 nm and a periodicity of 580 nm (a) without dye molecules on top, (b) 50 mM (c) 100 mM (d) 200 mM dye molecules on top. The used sample was sample #4 (see Table 4.1).

6.2.4 $\sqrt{c}$ dependence of the Rabi splitting

Table 6.1 and Figure 6.14 show the values for the Rabi splitting obtained by the fitting process for the arrays presented above. The splitting is the same as the coupling coefficient which was fitted in the fitting process and corresponds to the coupling strength. From Figure 6.14 it becomes obvious that the Rabi splitting of all three materials is proportional to $\sqrt{c}$, as expected theoretically. Figure 6.14 also shows the linear fits for the splitting. The fits are sufficient but since the lines cut the negative y-axis instead of going through the origin, one can assume that there is an offset. In addition, the linear fits for Au and Ge show deviations from the data points. One reason for this might be that the fits for 200 mM for Au and Ge were worse than the others (See Figures 6.11 and 6.12). The fit for a-Si is very good. Since the splitting increases with increasing dye concentration for all three materials, one can conclude that the systems of nanoarrays, dielectric and metallic, and emitters are in the strong coupling regime.

Material	50 mM splitting [eV]	100 mM splitting [eV]	200 mM splitting [eV]
Au	0.0699	0.1123	0.2041
Ge	0.0523	0.0815	0.1630
a-Si	0.0691	0.1009	1.563

Table 6.1: The values for the splitting obtained by the fitting process described in Section 5.4.

It remains to give an error estimation for the values of the splitting. One possibility is to repeat the fitting procedure for arrays of different periodicities and obtain a statistical error from there. In case of single measurements one could check the robustness of the fit. This can be done, for instance, by varying the absorption line of the emitter and see how strongly this affects the resulting values for the splitting.

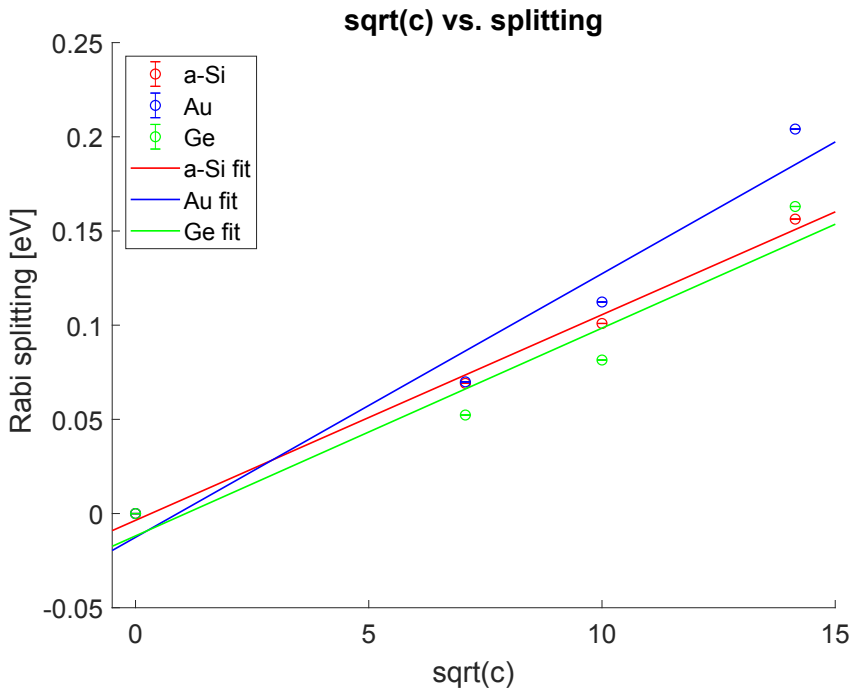

Figure 6.14: Splitting versus $\sqrt{c}$ for a-Si, Au and Ge. The solid lines refer to a linear fit done with Matlab. All three materials show the expected linear behaviour (see Equation 2.21).

Chapter 7

Conclusion

In this thesis, dielectric nanoparticle arrays made out of Ge and a-Si were fabricated and their dispersions without and with dye molecules were measured. In addition to this, Au nanoparticle arrays were fabricated and the same measurements were done.

The results of the dispersions of the bare arrays in Section 6.1 show that both metallic and dielectric nanoparticle arrays provide the expected behaviour of the SLRs as described in Section 3.2. The TE and TM modes are visible and with increasing periodicity the dispersion undergoes a redshift.

The comparison drawn between the dielectric and metallic nanoparticle arrays in Section 6.1.4 shows that the germanium nanoarrays provide slightly better results than the gold nanoarrays. Better means here, that the responses show a narrower linewidth. This can be seen by observing the msmallest Q-factors of the Ge nanoarrays which are higher by a factor of 1.27 for the in-plane wavevector at $k_y = 0$ and of 1.13 for $k_y = 0.5$. This is in accordance to the expected better performance of dielectric nanoparticles as described in Section 3.3. The smallest Q-factors for the Ge (Ti) samples were smaller than the smallest Q-factor of the Au nanoarrays by a factor of 1.20 and 1.24 for $k_y = 0$ and $k_y = 0.5$, respectively. This is due to the effects of the Ti, since it also responses to light and therefore makes the clean signal of the Ge nanoparticles more lossy. Unfortunately, Ge only nanoparticles prove to have a rather poor adhesion to the glass substrates, so depending on the application of the Ge nanoarrays one has to find a compromise between bad adhesion and good responses. However, it was still possible to do the strong-coupling measurements without the Ti lazer. At this point it is also important to note, that the Au nanoarrays also have a layer of Ti in order to improve the adhesion between substrate and nanoarrays. It is unknown, however, how much the Ti layer affects the responses of Au. It is known that it adds losses but maybe the effect is less than for Ge.

The smallest Q-factors of the a-Si nanoarrays are smaller than the smallest Q-factors of the Au nanoarrays by a factor of 1.19 and 1.29 for the in plane wavevector at $k_y = 0$ and $k_y = 0.5$, respectively. This is due to the fact that the RIE-process provides rather unreliable results as shown in Section 4.2.1. First of all, the aim was to fabricate cylindrical nanoparticles but due to the anisotropic etching, only cone shaped nanoparticles were fabricated. In addition, the nanoparticles do not seem to be uniformly, i.e. each particle is differently sized and shaped, and also their distance is not equally spaced. In addition, there are still residues of the a-Si between the particles (see Figure 4.5c). The transmission measurements in Section 6.1, however, show that although the quality of the a-Si nanoarrays is rather poor, they still provide responses as good as the GeTi nanoarrays. For example, the array with a nominal periodicity of 580 nm shows a FWHM of 13 meV (Q-factor of 109). Therefore, it is justifiable to expect results as good as or even better than the results achieved with the Ge and Au nanoarrays in case the a-Si nanoarrays are of good quality. In the inductively coupled plasma (ICP) RIE provides the possibility to obtain perfectly anisotropic etching of the a-Si through the Cr mask. In the ICP-RIE, the feed gas is ionized remotely away from the lower electrode by a second, independent RF-generator. Therefore, it is possible to control the plasma density independent to the forward power of the lower electrode. This leads to much higher anisotropy in the etching process but requires even more fine-tuning than the capacitively coupled plasma RIE used in this work [32].

The results of the dispersions measured with the dye molecules on top (see Section 6.2) show indications of strong coupling and the coupling strengths are similar for all materials. With increasing dye concentration, the bending of the upper branches of the TE modes becomes more and more visible. This is in accordance to the avoided crossing described in Chapter 2. In addition, in Section 6.2.4 the linear dependence of the Rabi splitting on the square root of the dye concentration is shown. Therefore, one can assume that the systems of the SLRs of Ge, Au and a-Si nanoparticle arrays are in the strong coupling regime with the dye molecules. Strong coupling between emitters and dielectric nanoarrays has not been observed before.

Since dielectric nanoarrays can provide narrower SLRs than metals due to their low-dissipative nature, the lifetimes of these states are much longer. The lifetime plays an important role in coherence phenomena and lasing. Therefore, the strongly coupled systems of dielectric nanoarrays and emitters could provide new developments and improvements in such applications.

In order to further improve the performance of the dielectric nanoparticle arrays, the diameter and height of the cylindrical nanoparticles needs to be optimized. This can be done experimenting or by numerical simulations, e.g.

with Lumerical. It might also be of interest to consider different nanoparticle shapes such as rods or other lattice geometries, e.g. hexagonal lattices.

Bibliography

[1] K Lance Kelly, Eduardo Coronado, Lin Lin Zhao, and George C Schatz. The optical properties of metal nanoparticles: the influence of size, shape, and dielectric environment. *The Journal of Physical Chemistry B*, 107(3):668–677, 2003.

[2] Vasyl G Kravets, Andrei V Kabashin, William L Barnes, and Alexander N Grigorenko. Plasmonic surface lattice resonances: A review of properties and applications. *Chemical Reviews*, 118(12):5912–5951, 2018.

[3] Baptiste Auguié and William L Barnes. Collective resonances in gold nanoparticle arrays. *Physical Review Letters*, 101(14):143902, 2008.

[4] Alex Krasnok, Martín Caldarola, Nicolas Bonod, and Andrea Alú. Spectroscopy and Biosensing with Optically Resonant Dielectric Nanostructures. *Advanced Optical Materials*, 6(5):1701094, March 2018.

[5] D Patrick O'Neal, Leon R Hirsch, Naomi J Halas, J Donald Payne, and Jennifer L West. Photo-thermal tumor ablation in mice using near infrared-absorbing nanoparticles. *Cancer Letters*, 209(2):171–176, 2004.

[6] Yu A Akimov, WS Koh, SY Sian, and S Ren. Nanoparticle-enhanced thin film solar cells: metallic or dielectric nanoparticles? *Applied Physics Letters*, 96(7):073111, 2010.

[7] Arseniy I. Kuznetsov, Andrey E. Miroshnichenko, Mark L. Brongersma, Yuri S. Kivshar, and Boris Luk'yanchuk. Optically resonant dielectric nanostructures. *Science*, 354(6314):aag2472, November 2016.

[8] Viktoriia E. Babicheva and Andrey B. Evlyukhin. Resonant Lattice Kerker Effect in Metasurfaces With Electric and Magnetic Optical Responses. *Laser & Photonics Reviews*, 11(6):1700132, November 2017.

[9] Andrey B Evlyukhin, Carsten Reinhardt, Andreas Seidel, Boris S Luk'yanchuk, and Boris N Chichkov. Optical response features of si-nanoparticle arrays. *Physical Review B*, 82(4):045404, 2010.

[10] P Törmä and W L Barnes. Strong coupling between surface plasmon polaritons and emitters: a review. *Reports on Progress in Physics*, 78 (1):013901, January 2015.

[11] Sergey I Bozhevolnyi, Luis Martin-Moreno, and Francisco Garcia-Vidal. *Quantum Plasmonics*, chapter 6. Springer, 2017.

[12] A. I. Väkeväinen, R. J. Moerland, H. T. Rekola, A.-P. Eskelinen, J.-P. Martikainen, D.-H. Kim, and P. Törmä. Plasmonic Surface Lattice Resonances at the Strong Coupling Regime. *Nano Letters*, 14(4):1721–1727, April 2014.

[13] L Shi, TK Hakala, HT Rekola, J-P Martikainen, RJ Moerland, and Päivi Törmä. Spatial coherence properties of organic molecules coupled to plasmonic surface lattice resonances in the weak and strong coupling regimes. *Physical Review Letters*, 112(15):153002, 2014.

[14] Mohammad Ramezani, Alexei Halpin, Antonio I Fernández-Domínguez, Johannes Feist, Said Rahimzadeh-Kalaleh Rodriguez, Francisco J Garcia-Vidal, and Jaime Gómez Rivas. Plasmon-exciton-polariton lasing. *Optica*, 4(1):31–37, 2017.

[15] Tim Byrnes, Na Young Kim, and Yoshihisa Yamamoto. Exciton–polariton condensates. *Nature Physics*, 10(11):803, 2014.

[16] Réjean Baribeau. Light-matter interaction volume 1 fundamental and applications. *Color Research & Application: Endorsed by Inter-Society Color Council, The Colour Group (Great Britain), Canadian Society for Color, Color Science Association of Japan, Dutch Society for the Study of Color, The Swedish Colour Centre Foundation, Colour Society of Australia, Centre Français de la Couleur*, 30(5):393–394, 2005.

[17] Wolfgang Fritzsche and Marc Lamy de la Chapelle. *Molecular Plasmonics*. John Wiley & Sons, Incorporated, Weinheim, GERMANY, 2014. ISBN 978-3-527-64971-6.

[18] Philip Hofmann. *Solid state physics: an introduction*. John Wiley & Sons, 2015.

[19] Anatoly V Zayats and Igor I Smolyaninov. Near-field photonics: surface plasmon polaritons and localized surface plasmons. *Journal of Optics A: Pure and Applied Optics*, 5(4):S16–S50, July 2003.

[20] Eliza Hutter and Janos H Fendler. Exploitation of localized surface plasmon resonance. *Advanced materials*, 16(19):1685–1706, 2004.

[21] Lukas Novotny. Effective wavelength scaling for optical antennas. *Physical Review Letters*, 98(26):266802, 2007.

[22] Weijia Wang, Mohammad Ramezani, Aaro I Väkeväinen, Päivi Törmä, Jaime Gómez Rivas, and Teri W Odom. The rich photonic world of plasmonic nanoparticle arrays. *Materials Today*, 2017.

[23] TK Hakala, HT Rekola, AI Väkeväinen, J-P Martikainen, M Nečada, AJ Moilanen, and P Törmä. Lasing in dark and bright modes of a finite-sized plasmonic lattice. *Nature Communications*, 8:13687, 2017.

[24] Baptiste Auguié, Xesús M Bendana, William L Barnes, and F Javier García de Abajo. Diffractive arrays of gold nanoparticles near an interface: Critical role of the substrate. *Physical Review B*, 82(15): 155447, 2010.

[25] N Papanikolaou. Optical properties of metallic nanoparticle arrays on a thin metallic film. *Physical Review B*, 75(23):235426, 2007.

[26] Keisuke Nakayama, Katsuaki Tanabe, and Harry A Atwater. Plasmonic nanoparticle enhanced light absorption in GaAs solar cells. *Applied Physics Letters*, 93(12):121904, 2008.

[27] David E Aspnes and AA Studna. Dielectric functions and optical parameters of Si, Ge, GaP, GaAs, GaSb, Inp, InAs, and InSb from 1.5 to 6.0 ev. *Physical Review B*, 27(2):985, 1983.

[28] Robert L Olmon, Brian Slovick, Timothy W Johnson, David Shelton, Sang-Hyun Oh, Glenn D Boreman, and Markus B Raschke. Optical dielectric function of gold. *Physical Review B*, 86(23):235147, 2012.

[29] Ye Feng Yu, Alexander Y Zhu, Ramón Paniagua-Domínguez, Yuan Hsing Fu, Boris Luk'yanchuk, and Arseniy I Kuznetsov. High-transmission dielectric metasurface with 2π phase control at visible wavelengths. *Laser & Photonics Reviews*, 9(4):412–418, 2015.

[30] Milton Kerker, D-S Wang, and CL Giles. Electromagnetic scattering by magnetic spheres. *JOSA*, 73(6):765–767, 1983.

[31] Jiaqi Li, Niels Verellen, and Pol Van Dorpe. Engineering electric and magnetic dipole coupling in arrays of dielectric nanoparticles. *Journal of Applied Physics*, 123(8):083101, February 2018.

[32] Fouad Karouta. A practical approach to reactive ion etching. *Journal of Physics D: Applied Physics*, 47(23):233501, 2014.

[33] PH Yih, V Saxena, and AJ Steckl. A review of SiC reactive ion etching in fluorinated plasmas. *Physica Status Solidi (b)*, 202(1):605–642, 1997.

[34] Aleksandr Kravchenko, Andriy Shevchenko, Victor Ovchinnikov, Arri Priimagi, and Matti Kaivola. Optical interference lithography using azobenzene-functionalized polymers for micro-and nanopatterning of silicon. *Advanced Materials*, 23(36):4174–4177, 2011.

[35] Henri Jansen, Han Gardeniers, Meint de Boer, Miko Elwenspoek, and Jan Fluitman. A survey on the reactive ion etching of silicon in microtechnology. *Journal of Micromechanics and Microengineering*, 6(1): 14, 1996.

[36] Sigma Aldrich Poly(methyl methacrylate). `https://www.sigmaaldrich.com/catalog/product/aldrich/182230?lang=en&region=GB`. Accessed: 2018-10-25.

[37] Sigma Aldrich Anisol. `https://www.sigmaaldrich.com/catalog/product/SIAL/296295?lang=en&region=GB`. Accessed: 2018-10-25.

[38] Sigma Aldrich Ir-792 perchlorate. `https://www.sigmaaldrich.com/MSDS/MSDS/DisplayMSDSPage.do?country=GB&language=EN-generic&productNumber=425982&brand=ALDRICH&PageToGoToURL=https%3A%2F%2Fwww.sigmaaldrich.com%2Fcatalog%2Fproduct%2Faldrich%2F425982%3Flang%3Dde`. Accessed: 2018-10-25.

[39] Meizhong Wang. *Understandable electric circuits*, chapter 10. The Institution of Engineering and Technology, 2010. ISBN 9781849191142.